

Microwave-Induced Transitions in a Hybrid Double Quantum Dot



Master thesis
written by *Judith T. Suter*
supervised by *Charles M. Marcus*
University of Copenhagen
August, 2018

Faculty: Faculty of Science
Institute: Niels Bohr Institute
Author: Judith Tabea Suter
Email: hlb643@alumni.ku.dk
Title: Microwave-induced transitions in a hybrid double quantum dot
Supervisor: Charles M. Marcus
Handed in : August 5th, 2018

Contents

1.0	Acknowledgements	iv
1.1	Abstract	1
1.2	Theory	2
1.2.0	Technological Revolution	2
1.2.1	DiVincenzo Criteria	2
1.2.2	Majorana Fermions	3
1.2.3	Superconductivity	5
1.2.4	Majorana Bound States in Solid State Physics	6
1.2.5	Andreev Reflections and Andreev Bound States	8
1.2.6	Topological Transitions	10
1.2.7	Coulomb Blockade in Semi- and Superconducting Quantum Dots	10
1.2.8	Magnetic Field Evolution of Superconductors	13
1.2.9	Coupled Quantum Dot Systems	14
1.2.10	Photon Assisted Tunneling in a Double Quantum Dot	16
1.3	Materials and Methods	18
1.3.0	Superconducting Double Island Device	18
1.3.1	Device Fabrication	19
1.3.2	Measurement Setup	22
1.3.3	Measurement Techniques	23
1.4	Results and Discussion	29
1.4.0	Aligning the Magnetic Field along the Nanowire	29
1.4.1	Initial Characterization	30
1.4.2	Hunting in Bias Spectroscopy	31
1.4.3	Magnetic Field Evolution in Charge Sensing	35
1.4.4	Photon Assisted Tunneling	36
1.4.5	Photon Assisted Tunneling in Absence of an External Magnetic field.	40

1.4.6	Photon Assisted Tunneling at Finite Magnetic field.	44
1.5	Conclusion	48
1.6	Outlook	49
	Appendices	51
A	Fabrication of Double Island Device	51
B	Photon assisted tunneling	55

1.0 Acknowledgements

I thank Charles M. Marcus for showing how to set scientific goals and follow through with curiosity, dedication and attention to detail while never losing track of the bigger picture. Leading by example, he also demonstrates how to captivantly talk about research to any audience. I am grateful for all the possibilities and responsibilities he has given me.

I thank Deividas Sabonis and David van Zanten with whom the experiment presented in this thesis was conducted. Their inexhaustible passion for physics created the educational environment that guided and inspired me throughout this project. Spending the past year with them around the cryostat 'little snowman' while exploring and discussing has been an invaluable, captivating journey.

I thank Dmitry Pikulin and Jukka Väyrynen for enlightening discussions over Skype and Spanish omelet which provided the theoretical backbone for this work.

I further want to thank all the wonderful people at QDev for providing constructive feedback, discussions, sugar highs with countless cakes, for leaving cheesy inspirational quotes on my desk, taking me out for seaweed-themed picnics and happy tea breaks. While all members of QDev shaped my time here into a unique experience, I want to take this occasion to express my gratitude to a few people in particular.

I thank:

Mingtang Deng, a triple thread of scientific brilliance, kindness and wit, for initially introducing me to the fascinating universe evolving around fab and fridges with the support of Saulius and Gerbold.

Saulius Vaitiekėnas, for explaining topology to me with a hair-ribbon in the very beginning and demonstrating the same smart creativity in supporting me through fab, fridge or theory challenges ever since.

Gerbold Menard for arguably the most artistic proofreading remarks I have ever received falling in line with his many illustrative explanations helping me debug and battle countless computer, cleanroom and conceptual crises.

Shivendra Upadhyay for his knowledgeable all-around guidance and always spreading happiness with his sharp mind and exquisite collection of bold socks.

Eoin O'Farell and Dovydas Radzmaze for passing on their widespread skills and knowledge while transitioning from being fridge neighbors to becoming one big experimental physics family.

Anasua Chatterjee, Filip Křížek, Alexander Whitar and Gian-Luca Anselmetti for their

helpful, constructive and encouraging remarks on this documents.

Finally, my parents and sister for being uniquely wonderful people.

I gratefully acknowledge the financial support I have received in connection with my scholarship from the Werner Siemens Foundation.

1.1 Abstract

The research field of Majorana fermions, exotic particles that are their own antiparticles, has evolved from being a purely theoretical entity to experimental relevance within less than a decade. Following theoretical proposals [1],[2] experimental signatures consistent with Majorana bound states have been observed in hybrid materials [3], [4], [5], [6]. Due to the topologically protected nature of these quasi particle excitations, they constitute a promising platform for intrinsically fault-tolerant quantum computing.

The motivation of this work is to probe the tunnel coupling between two Majorana bound states across a controllable junction. This would extend previous work probing the tunnel coupling between two charge states using microwave spectroscopy on semiconducting quantum dots [7], [8] and a Cooper pair box [9].

This thesis presents measurements of Cooper-pair and single electron tunneling across a Josephson junction in a quasi one-dimensional hybrid system with a mesoscopic double island geometry. Magnetic field evolution demonstrates a change in Coulomb blockade periodicity from $2e$ to $1e$ *via* an even-odd regime. This transition occurs well below the critical field of the system. Under microwave irradiation photon assisted tunneling is observed both in absence and presence of an axial magnetic field. The Josephson coupling energy E_J at $B=0$ and the $1e$ coupling strength E_{1e} at $B = 750$ mT are determined by extracting the frequency-dependence of the position of microwave-induced transition resonances. Corresponding transport measurements at finite magnetic field show a zero bias conductance peak extended in gate voltage and separated from the quasiparticle continuum by a superconducting gap. Results are consistent with single electron tunneling between two zero energy quantum states residing on each side of the Josephson junction.

1.2 Theory

1.2.0 Technological Revolution

During the course of the last century computational power rapidly increased fueling a comprehensive revolution of the world's social and technological infrastructure. Back in 1965 Gordon Moore anticipated this computational boom based on his prediction – known as Moore's law – that the feasible number of transistors per area would double every two years [10]. Transistors are binary building blocks for computation and data storage. In classical computation they are referred to as bits and can be regarded as basic switch elements, whose states – on or off – can be expressed as a logical 0 or 1. This far, rapidly advancing material science and engineering capabilities have been able to keep up with Moore's law. The downscaling of these classical transistors however, can not be perpetuated *ad infinitum*. Approaching the atomic scale constitutes the lower limit since in this regime the quantum mechanical behavior of matter becomes relevant.

The theory of quantum mechanics contains counterintuitive concepts of superposition and entanglement of states which could be exploited in quantum computers as first introduced by Richard Feynman [11]. Corresponding quantum bits hereafter, referred to as qubits, could be in a superposition of 0 *and* 1 simultaneously. This parallelism makes the computation capability of quantum computers grow exponentially with every additional qubit while classical computers are conditioned to linear growth with addition of each bit.

Quantum computers are predicted to enable the simulation of quantum mechanical systems, which could ultimately promote a variety of other research fields. However, as with all leaps in history, the true allure of quantum computing is that its potential and implications are intangible until the era it induced arrives.

1.2.1 DiVincenzo Criteria

In order to implement a quantum computer, a set of universal criteria needs to be fulfilled as declared by David DiVincenzo and Daniel Loss [12]. To begin with, one needs two well distinguishable levels in a quantum system. These can for example be implemented by lifting the spin degeneracy in a spin-full system under an external magnetic field (see Fig. 1.1 1). Further, the system needs to be initialized in a distinct ground

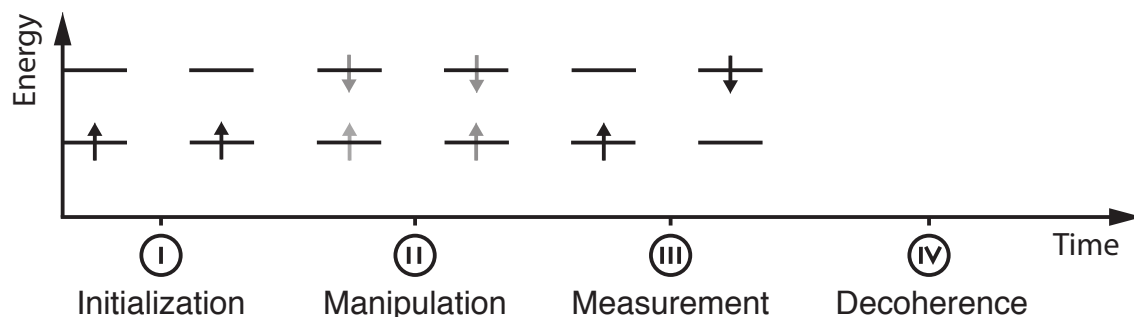


Figure 1.1: DiVincenzo criteria: A set of two well-defined two-level systems of spin split energy states is initialized into its ground state (I). Turning on an exchange coupling superposes the states and logical gate operations can be performed (II) before the system is projected onto a state during the measurement (III). These three steps have to be completed within the coherence time of the system in order to maintain its encoded information (IV).

state. Employing external triggers or exceeding the state relaxation time can transition an excited system into its ground state. A third criterion states that a series of logical gate operations have to be applicable. This constitutes the computation step during which logical gate operations coherently manipulate the quantum state (see Fig. 1.1 II). Finally, the measurement process has to be completed within the coherence time of the system (see Fig. 1.1 III, IV). The coherence time denotes the time span over which the encoded information of the system is maintained and therefore computation can be done. When exceeded, the encoded information is lost due to interactions of the system with its environment.

One approach to establish long coherence times for quantum computation evolves around a theoretically predicted particle – the Majorana fermion – which would be intrinsically protected against decoherence.

1.2.2 Majorana Fermions

Delocalized particles called Majorana fermions (MFs) have been theoretically predicted for which local environmental perturbations would not destroy their quantum state. Therefore, MFs have been proposed as a promising basis for quantum computing.

Ettore Majorana, the eponym of the exotic particles found MFs as a real solution of the Fermi-Dirac equation. A MF differs from a Dirac fermion in that it is its own

antiparticle. The neutral state has to reside at zero energy since it is an equal superposition of electron and hole [13]. This can be expressed using the Majorana operators γ_1 and γ_2 and the fermionic annihilation and creation operators c and c^\dagger :

$$\gamma_1 = c^\dagger + c \quad (1.1)$$

$$\gamma_2 = i(c^\dagger - c) \quad (1.2)$$

MFs emerge in pairs. When in close proximity to each other their wavefunctions overlap and their degeneracy is lifted which projects them onto their fermionic state $n = c^\dagger c$, which can either be occupied or empty. This decides over the parity of the system. The sum over all fermionic states in a system $\sum_{i=1}^N n_i$ can either have even or odd parity constituting the quantum mechanical two-level system [13].

Ordinary fermions can be expressed as a combination of two localized Majoranas.

$$c^\dagger = \frac{\gamma_1 + i\gamma_2}{2} \quad (1.3)$$

$$c = \frac{\gamma_1 - i\gamma_2}{2} \quad (1.4)$$

A system with $2N$ MFs (where N is integer) can therefore give rise to N ordinary fermions with a 2^N -fold degenerate ground state. In order to implement a topological qubit N has to be at least 2. Then, both parity states are double-degenerate [14] forming an even parity ground state ($|00\rangle, |11\rangle$) and an odd parity ground state ($|10\rangle, |01\rangle$) [13]. Information can be encoded quantum mechanically due to the non-trivial exchange statistics of MFs.

When the unitary exchange operator \hat{P} is applied to two ordinary identical particles in the state $|\Psi(x_1, x_2)\rangle$, the wavefunction remains invariant for bosonic states and picks up a minus sign if the particles are of fermionic nature ($\pm |\Psi(x_2, x_1)\rangle$). In two dimensional space, applying \hat{P} twice on both fermions and boson returns the original state with an addition phase pickup ϕ , $|\Psi(x_1, x_2)\rangle e^{i\phi}$, which in itself is not a system suitable for quantum computations. This differs for MFs: They are non-Abelian particles and as such their exchange statistics are non-trivial. Circling one MF around another one transfers the system between degenerate ground states in addition to the trivial phase pickup. The final wavefunction encodes the information of the trajectory of the MFs.

These particle exchange processes – referred to as braiding – constitutes the basic operating scheme for topological quantum computation.

In order for MFs to gain experimental relevance they have to be delocalized, meaning spatially separated from each other to avoid any coupling. Only then could the non-Abelian statistics of MFs be exploited as a promising platform for quantum computing. Extending Majoranas work, Alexei Kitaev introduced a one-dimensional tight binding model with superconducting electron pairing. In the trivial case two MFs residing on the same site pair up which describes a system with one fermion per site. A pairing of MFs from neighboring sites gives rise to unpaired, non-localized MFs at the ends of the system which theoretically could be employed for quantum computation [15]. Superconductors are a self-evidently a central element in efforts to adapt Kitaev's toy model for an experimental system.

1.2.3 Superconductivity

Superconductivity is defined as a phase that particular materials can transition into when cooled below a characteristic critical temperature T_C . There, the system can pass dissipationless current which is quantized in units of $2e$, where e is the electron charge. In efforts to explain the peculiar characteristics of superconductors John Bardeen, Leon Cooper and John Schrieffer presented a microscopic theory of superconductivity based on finite attraction induced electron pairing [16].

A single electrons moving through the crystal lattice has attractive interactions with positively charged ions. The resulting lattice deformation gives rise to phononic excitations attracting an addition electron, which – mediated by electron-lattice interactions – experiences a finite attractive force with the first electron. The two electrons pair up to form a Cooper pair (CP)[17]. Each electron possesses half-integer spin which results in a quasiparticle with effective integer spin and charge $2e$. The spin quantum number of the two paired electrons can either be 0 when the spins are in an antisymmetric singlet state or 1 when the spin projections are co-aligned in the symmetric triplet state. Depending on the spin projection alignment, the distinction between s-wave (singlet) and p-wave (triplet) superconductivity is made [17].

CPs have bosonic properties due to their integer spin and can therefore condense

into a quantum mechanical ground state. The CP condensate is energetically separated from single electron quasiparticle excitations by a superconducting gap Δ . In order to break up a CP, a minimum energy of 2Δ has to be supplied to create two electrons populating the quasiparticle continuum.

Superconductivity imposes particle-hole symmetry. Single electrons and holes can lower their energy by combining to form so-called Bogoliubov quasiparticles and enter the superconducting gap. Zero-energy quasiparticles which are equal parts hole and electron have the same topological properties as the theoretically predicted Majorana Fermions and are referred to as Majorana bound states [13]. Superconductors therefore constitute a crucial ingredient to engineer a solid state system that can host Majorana bound states.

1.2.4 Majorana Bound States in Solid State Physics

Transferring Kitaev's theoretical tight-binding toy model [15] – based on spinless superconducting p-wave pairing – onto a solid state system requires advanced material engineering since experimentally only s-wave superconductors are accessible. Theoretical blueprints made it is feasible to implement an effective p-wave superconductor when four key ingredients are present in a system [1], [2].

Firstly, a one dimensional crystal with a spin degenerate parabolic energy dispersion is required. Secondly, the material needs to have strong Rashba spin-orbit coupling. The interaction of the orbital motion of an electron and an electrostatic field induces a momentum k dependent Zeeman energy referred to as spin-orbit coupling [18]:

$$H_{SO} \approx \mu_B (E \times k) \frac{\sigma}{mc^2}, \quad (1.5)$$

where μ_B is the Bohr magneton, E is the electric field given by the crystal potential, k is the momentum, σ denotes the vector of the Pauli matrices, m the mass of the electron and c the speed of light. Spin-orbit interactions lift the spin degeneracy by shifting the spin up and spin down parabolas in opposite directions in k -space [19]. At their intersection point at $k = 0$, however, they remain spin degenerate. Spin-orbit coupling also introduces a zero-point energy offset corresponding to the spin-orbit energy. A parallel external magnetic field B introduces an anti-crossing at $k = 0$ when it is applied parallel to the one-dimensional crystal and perpendicular to the Rashba spin-orbit field.

$$E_Z = g\mu_B B, \quad (1.6)$$

where g denotes the Lande g -factor. Finally, to introduce particle-hole symmetry and to open up an energy gap around the Fermi level an s-wave superconductor is coupled to the semiconductor system by proximity. The extension of the superconducting properties across the superconducting-normal interface is known as the proximity effect (see Sec. 1.2.5) [20].

For the system to host MBSs it has to transition from the trivial to the topological phase, the condition for which is:

$$E_Z > \sqrt{\mu^2 + \Delta^2}, \quad (1.7)$$

Adjusting either the chemical potential μ or the magnetic field such that the energy band gap closes and reopens transitions the system into the topological phase yielding MBSs at its ends.

The Zeeman field B driving the topological transition is compromising superconductivity. If B exceeds a critical value B_C superconductivity will break down. In order to transition into the topological regime below B_C , the effective g -factor (Eq. 1.6) needs to be large. The g -factor of the proximity-induced semiconductor depends on the charge carrier density which is gate-tunable [21].

To experimentally probe for the presence of subgap states, a tunneling barrier can be imposed between the superconducting material and a normal lead. In the tunneling regime the current is proportional to the local density of states [22]. Experimental observations of a MBSs in this configuration are feasible since single electrons are allowed to tunnel between a lead and a MBS which is charge neutral [23].

Experimental signatures of MBSs were first observed by Mourik *et. al.* in an indium antimonide (InSb) nanowire-based device partially covered by the superconductor aluminum (Al) [3]. Tunneling bias spectroscopy of the magnetic field evolution demonstrates the emergence of a zero-bias peak (ZBP). The ZBP persists as a function of B and gate voltages. They further observed, that the ZBP is absent when one of the introduced conditions for a topological phase transition is omitted. This and subsequent

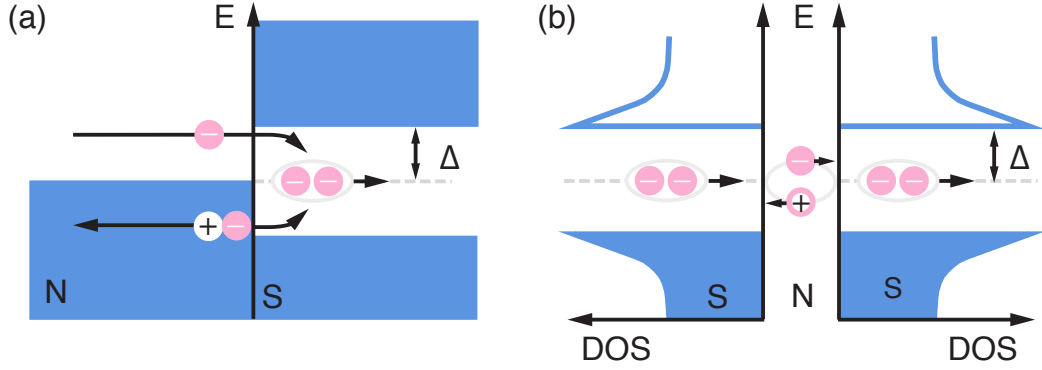


Figure 1.2: Andreev reflections: a) Andreev reflections at a normal (N)-superconducting (S) interface. b) Cyclic Cooper pair transport through an S-N-S junction.

experiments provide compelling evidence that MBSs have been observed. Quantized conductance of the ZBP as well as the closing and reopening of the superconducting gap coinciding with the emergence of the ZBP have been reported [6], [21], [24]. However, presumably only the demonstration of non-Abelian of zero energy states could confirm Majorana bound states unambiguously. Based on theoretical simulations it has been shown that trivial bound states in an inhomogeneous potential environment can also give rise to the observed Majorana characteristics [25]. These trivial subgap states are so-called Andreev bound states.

1.2.5 Andreev Reflections and Andreev Bound States

Interesting physical phenomena emerge when a superconductor is brought into contact with a non-superconducting system, hereafter referred to as normal phase. An electron with energy $E < \Delta$ propagating in the normal phase towards the superconducting interface is energetically not allowed to be transmitted into the superconducting energy gap as a single particle. The electron can either be reflected or combine with an additional electron of opposite spin and momentum to form a CP and be transmitted to populate the Bose-Einstein condensate inside the superconducting gap (see Fig. 1.2 a) [26]. In case of the latter, a hole with the same momentum and opposite spin is retro-reflected to conserve momentum. Analogously, a hole with $E < \Delta$ can also be transmitted from the normal into the superconducting phase causing a CP to enter the normal phase. These retro-reflections of electrons and holes associated with Cooper pair transfer across an

superconducting-normal interface are referred to as Andreev reflection. Andreev reflections of holes are the underlying mechanism allowing for the normal state material in hybrid systems with superconductors to be proximitized by Cooper pairs 'leaking' into the semiconductor [20].

Based on the same physical mechanism two superconductors separated by a normal phase 'weak link' can exchange CPs across the junctions in form of a dissipationless supercurrent (see Fig. 1.2 b). Coherent control over such superconducting-normal-superconducting systems has been demonstrated [27], [28].

Supercurrent is driven by a difference in the superconducting phase of the two separated segments $\Delta\Phi = \Phi_1 - \Phi_2$. The electrons (holes) acquire a phase of $\Delta\Phi_1$ or Φ_2 ($-\Phi_1$ or $-\Phi_2$) with every Andreev reflection adding up to a phase dependence on $\Delta\Phi$ after completing one cycle. This gives rise to resonant standing waves bound between two N-S interfaces. The emerging low-lying energy modes are referred to as Andreev bound states (ABSs). ABSs come in pairs due to particle-hole symmetry. For weak link elements shorter than the superconducting coherence length, the energies $\pm E_{ABS}$ of an ABS in a single channel are symmetric with respect to the Fermi energy [29]:

$$\pm E_{ABS} = \Delta \sqrt{1 - \tau \sin^2 \frac{\Delta\Phi}{2}}, \quad (1.8)$$

where τ is the transmission. These electron (hole) excitations form a discrete energy spectrum which is determined by $\Delta\Phi$ [30]. ABSs have been measured by tunneling spectroscopy in different weak link systems such as carbon nanotubes and graphene-based quantum dots coupled to two superconducting leads [31], [32]. The weak link is not only restricted to being a junction element in the conventional Cooper-pair box geometry but could also be a semiconducting nanowire segment in contact with a superconductor as in the system explored in this work.

The previously mentioned ongoing difficulty to distinguish MBSs from ABSs is partially caused by ABSs allowing single electron sub-gap population. Furthermore, based on simulations Lui *et. al.* demonstrated that the bending of ABSs caused by local impurities inside or in close proximity to the superconducting nanowire can lead to trivial ZBPs persisting in gate space and magnetic fields [25]. Their simulations are based on experimental results consistent with MBSs in a hybrid quantum dot reported by Deng *et. al.* [5].

MBSs – despite qualitatively similar signatures to trivial ABSs – only emerge when the system undergoes a topological phase transition.

1.2.6 Topological Transitions

The field of topology is concerned with the question of whether two states can continuously be transformed into one another. Hence, if properties of a system are preserved when it is subjected to deformation. One property for example could be the number of holes in a system. Entities with the same hole count represent one topological class.

A topological qubit would exploit this principle to protect the MBSs via electron-hole band inversion (as discussed in Sec. 1.2.4). Transitioning from the trivial to the topological phase can be done by changing the chemical potential or the magnetic field induced Zeeman splitting. The emergence of MBSs is predicted to coincide with the gap closing and re-opening resulting in its topological protection from local perturbations (see Sec. 1.2.4).

An important solid state structure to host and probe the presence of these topologically protected MBSs are quantum dots [5], [33].

1.2.7 Coulomb Blockade in Semi- and Superconducting Quantum Dots

A quantum dot (QD) is a spatially confined solid state structure defined and controlled by a minimum of three electrostatic gate electrodes: two cutter gates introducing tunable tunneling barriers which couple the QD to adjacent source and drain electrodes and a capacitively coupled plunger gate controlling the quantum mechanical states of the QD.

The device investigated in this thesis is based on QDs of semiconducting and superconducting nature. Semiconducting QDs have size-dependent, discrete energy level spacings, where each level can be occupied by up to two single electrons. QDs in the superconducting phase are characterized by the zero energy state of the CP condensate which is well separated from the quasiparticle continuum by the superconducting gap. Superconducting QD have parity-dependent energy states instead of a resolvable level

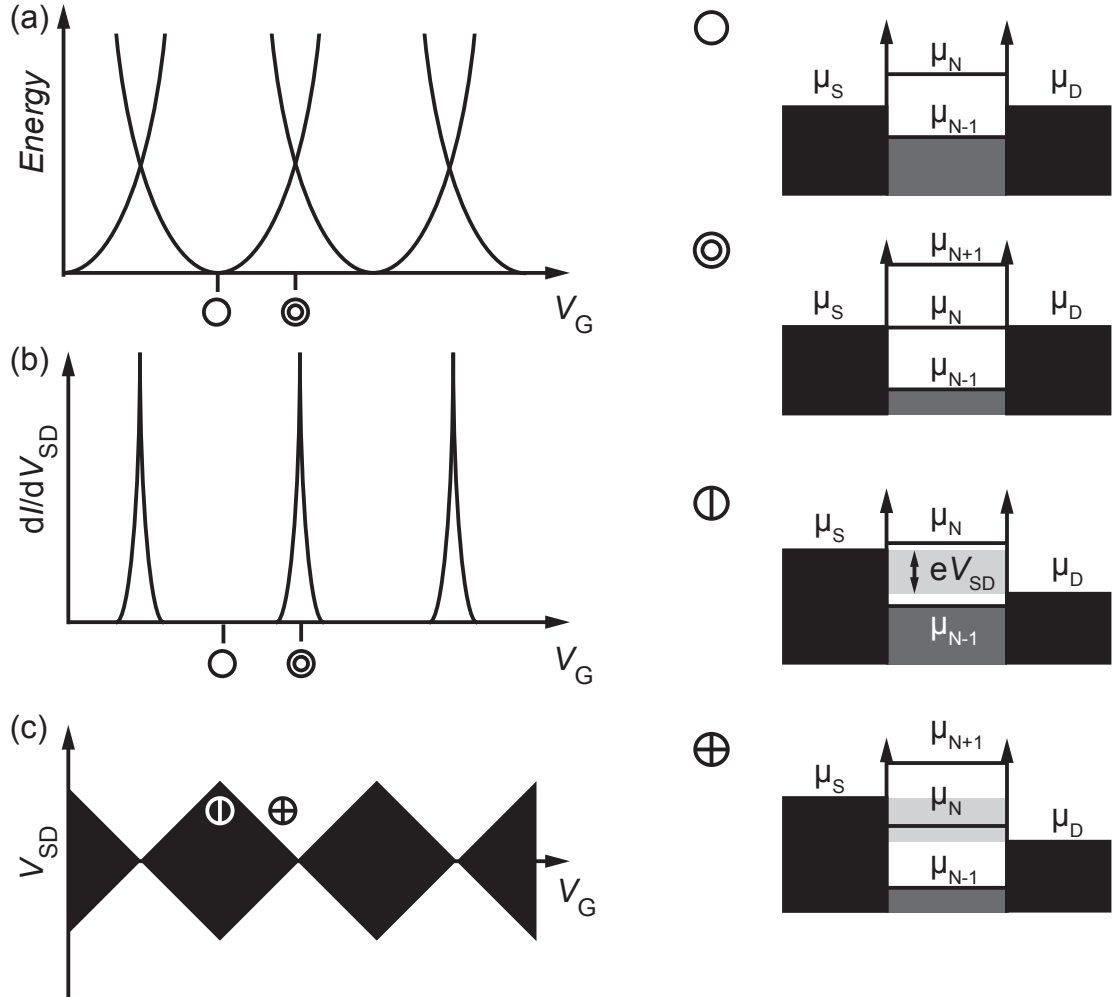


Figure 1.3: Schematic representation of a quantum dot. a) Energy dispersion as a function of gate voltage V_G . Sweeping V_G transitions the system between different ground states. b) Differential conductance dI/dV as a function of V_G . Electrons are only allowed to tunnel at the ground state degeneracy points where the differential conductance shows a resonance peak. c) Plotting the differential conductance as a function of source drain voltage V_{SD} and V_G reveals Coulomb diamonds. The black represents non-conductive Coulomb blockade. In the white regions at least one state lies in the source-drain bias window and electrons can flow from source to drain.

spacing. They can be characterized by discretized charge state excitations differing from each other by an integer multiple of the CP charge $2e$.

The quantization of the number N of electrons for a semiconducting (CPs for a superconducting) QD is established by imposing a capacitance C dependent charging energy E_C :

$$E_C = \frac{e^2}{2C} \quad (1.9)$$

In the operating regime of a QD the charging energy dominates as $E_C \gg k_B T, V_{SD}, \tau$, where $k_B T$ is the thermal energy, V_{SD} the source-drain bias voltage and τ lifetime broadening of the QD state arising from coupling to the environment.

The total electrostatic energy of the system depends on the charge of the QD and the gate induced charge. The charge of the QD is defined as $Q = N \cdot q$, where N is the number of electrons (CPs) and q denotes the charge of the particles. The gate induced energy contribution is given by $n = V_g q_g$ with voltage V_g and q_g being the charge residing on the plunger gate [19]. The total electrostatic energy can therefore be defined as:

$$E(n) = \frac{Q^2}{2C_\zeta} - n^2 \quad (1.10)$$

This gives rise to a parabolic energy dispersion (see Fig. 1.3 a).

To describe tunneling processes and quantum transport an electrochemical potential μ of the QD is introduced which corresponds to the energy required to add an electron (CP). For a QD with $N-1$ electrons (CPs), the electrochemical potential for adding an N th electron (CP) is given by the energy difference between the lowest unoccupied and the highest occupied energy state E_N, E_{N-1} [19]:

$$\mu_N(V_G) = E_N(V_G) - E_{N-1}(V_G) \quad (1.11)$$

The relationship between μ_N and the chemical potentials of source and drain electrodes, μ_S and μ_D , determines if current can flow through the system. The differential conductance dI/dV as a function of V_G reveals the Coulomb blockaded nature of the system (see Fig. 1.3 b). E_C is only overcome when μ_N is on resonance with the leads ($\mu_S = \mu_N = \mu_D$). Then, current can flow resulting in a peak in differential conductance.

For V_g values corresponding to off-resonance configurations ($\mu_{S,D} \neq \mu_N$) the system is in non-conductive Coulomb blockade. This allows for controlled manipulation of the charge occupation of a QD *via* the plunger gate voltage V_G [34].

Measuring the differential conductance not only as a function of the gate potential but also source-drain bias voltage ($-|e|V_{SD} = \mu_S - \mu_D$) shows Coulomb diamonds (see Fig. 1.3 c). At small source drain bias voltages ($\mu_S > \mu_D$) electrons (CPs) can tunnel on and off the QD for a V_G interval where $\mu_S \geq \mu_N(V_G) \geq \mu_D$ [19]. Increasing the source-drain voltage bias ($\mu_S \gg \mu_D$) eventually transitions the system into a regime of finite conduction over the entire V_g space.

Superconducting quantum dots demonstrate a generic change in Coulomb blockade peak spacing as a function of magnetic field.

1.2.8 Magnetic Field Evolution of Superconductors

Superconducting systems transition from $2e$ to a $1e$ periodic Coulomb blockade peak spacing under the influence of an external magnetic field (see Fig. 1.4 a). Transport in the superconducting ground state for low field values is mediated by Cooper pairs and the Coulomb blockade is $2e$ periodic in gate voltage V_G (see Fig. 1.4 b I). The $1e$ periodic parabolas – charge states of an integer multiple of $1e$ – are energetically well separated from the CP condensate by the superconducting gap Δ . Increasing the magnetic field in a Coulomb blockaded system lowers the zero-point energy of the $1e$ parabolas. As soon as they descend below the degeneracy point of two neighboring $2e$ parabolas – marking the charging energy E_C of the superconducting system – they introduce new ground states (see Fig. 1.4 b II,III). This enters the system into the even-odd regime and two neighboring charge states differ by a single electron. Finally, once the zero point energies of even and odd charge states are degenerate the system is in the $1e$ periodic regime (see Fig. 1.4 b IV).

The emergence of zero bias single electron transport *via* an even-odd regime in a superconductor-semiconductor hybrid system as the one investigated can occur either due to quenching of the proximity-induced superconductivity, in the presence of Andreev bound states residing below E_C or at the topological phase transition where Majorana bound states emerge.

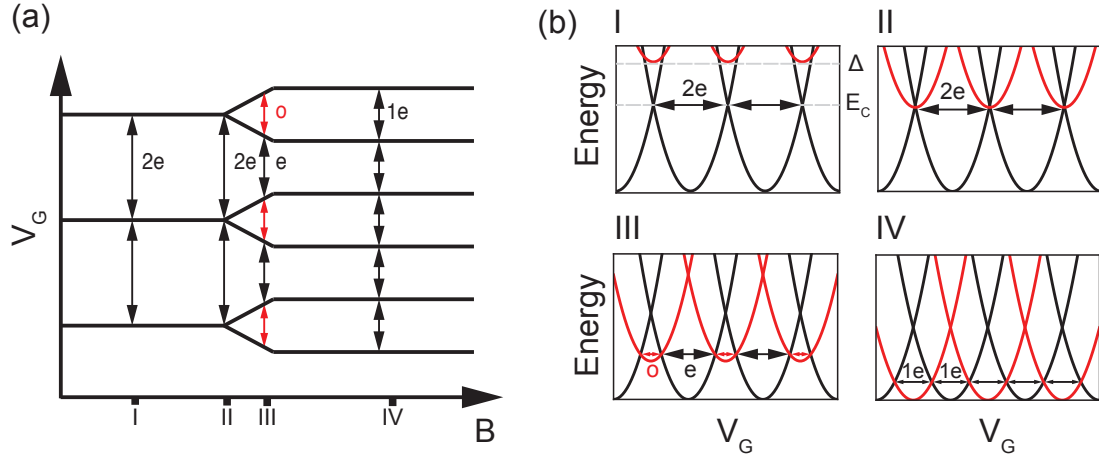


Figure 1.4: Transitions from $2e$ to $1e$ periodic Coulomb blockade: a) Charge state transitions as a function of gate voltage V_g and magnetic field B indicating a periodicity change at finite field from $2e$ to $1e$ via an even-odd regime. b) Energy dispersion as function of gate voltage at different values of B . At low values of B the system is in $2e$ periodic Coulomb blockade (I). Increasing B lowers the zero-point energy of the $1e$ periodic states (red). When they cross the degeneracy point of the even ground states (II) the system transitions into an even (e) and odd (o) regime (III) before eventually the odd parabolas become degenerate with the even ones and the Coulomb blockade of the system is $1e$ periodic at high fields (IV).

1.2.9 Coupled Quantum Dot Systems

Bringing two QDs into close proximity couples them capacitively and via tunnel-coupling [19]. The electrochemical potentials of the left and right QDs, μ_L and μ_R , depend on the number of electrons (CPs for superconducting QDs) N_L , N_R residing on them. The charging energies of the two QDs are [35]:

$$E_{CL} = \mu_L(N_L + 1, N_R) - \mu_R(N_L, N_R) \quad (1.12)$$

$$E_{CR} = \mu_R(N_L, N_R + 1) - \mu_L(N_L, N_R) \quad (1.13)$$

In addition to the charging energies of the individual QDs, their coupling gives rise to a mutual charging energy, E_{CM} , accounting for changes in energy of one QD when the electron occupation of the other one changes [35]:

$$E_{CM} = \mu_L(N_L, N_R + 1) - \mu_L(N_L, N_R) = \mu_R(N_L + 1, N_R) - \mu_R(N_L, N_R) \quad (1.14)$$

Sweeping plunger gate voltages, V_{LP} and V_{RP} , changes the electrochemical poten-

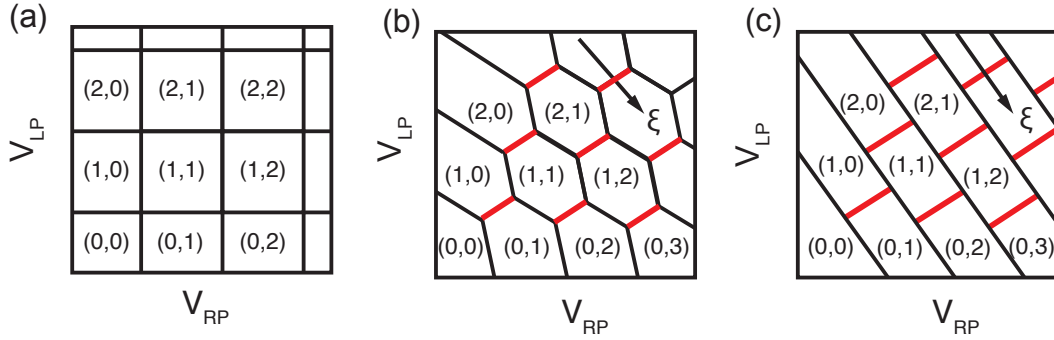


Figure 1.5: Charge stability diagram for double quantum dot for different inter-island coupling strengths: a) No coupling. b) Finite coupling. c) Strong coupling. QD-lead transition are represented in black, inter-QD transitions are highlighted in red. Figure adapted from [35]

tial of the respective Coulomb blockaded QD bringing it onto and off resonance with the electrochemical potentials of the other QD and the leads. In the absence of a source drain bias voltage transport only occurs when both islands are simultaneously on resonance with each other and the leads ($\mu_s = \mu_L = \mu_R = \mu_D$). These so-called triple points outline the intersections of a periodic honeycomb structure referred to as charge stability diagram. Each hexagon represents a subspace in gate voltages where the charge state of the double QD is fixed [19].

The coupling between the two QDs can be controlled by the tunneling barrier between them. The coupling is reflected in the shape of the charge state outlines in charge stability diagrams (see Fig. 1.5 a-c). Charge state degeneracy lines connecting triple points indicate either QD-lead or inter-QD charging events. For the system to transition between equi-charge states mediated by inter-QD tunneling events a trajectory along a compensated $V_{LP} - V_{RP}$ line-cut referred to as detuning axis ϵ can be defined (see Fig. 1.5 b,c). Moving along ϵ conserves the total charge of the double QD by redistributing one electron (CP) between the two QDs each time an inter-island transition is crossed.

The coupling of two adjacent equi-charge states can be probed using microwave irradiation giving rise to photon assisted tunneling.

1.2.10 Photon Assisted Tunneling in a Double Quantum Dot

In systems where electrons can coherently tunnel between the two QDs the corresponding equi-charge eigenstates $|0\rangle$ and $|1\rangle$ delocalize over the double quantum dot. The resulting hybridized eigenstates are coherent symmetric and anti-symmetric superpositions of the two initial states (see Fig. 1.6 a) [35]:

$$\Psi_{1,2} = \alpha |0\rangle \pm \beta |1\rangle \quad (1.15)$$

At equi-charge state degeneracy α and β converge to $\frac{1}{\sqrt{2}}$ and the hybridized states $\Psi_{1,2}$ are separated by an energy gap ΔE which is given by the coupling energy [36]. Corresponding charge stability diagrams also reflect the coupling strength in the rounding of the hexagons in case of a double quantum dot system (see Fig. 1.6 b, c). The energy dispersion of the hybridized states can be traced using photon assisted tunneling (PAT) [7], [9], [8].

PAT refers to inelastic electron (or CP) tunneling across a potential barrier facilitated by the absorption or emission of photons. The double QD is irradiated with a sinusoidal microwave signal. If the photon energy of the applied frequency $E = hf$, where h is Planck's constant, corresponds to the excitation energy between the ground and excited hybridized state ($\Delta E = E(\Psi_1) - E(\Psi_2)$) an electron (CP) can tunnel across the barrier (see Fig. 1.6 d) [37]. The energy splitting depends on the detuning position along ϵ . The tunnel coupling strength and is given by [9]:

$$\Delta E = \sqrt{E(\epsilon)^2 + E_{cpl}^2}, \quad (1.16)$$

where $E(\epsilon)$ accounts for the charging energies in the system (see Sec. 1.2.9) and the ϵ dependent energy dispersion. At detuning the excitation energy directly reflects the coupling strength. Microwave-induced transitions manifest themselves as additional peaks in charge stability diagrams appearing parallel to the inter-island transition line shifted along ϵ . The microwave-induced resonances are absent for uncoupled systems (see Fig. 1.6 e, f) [8]. The frequency-dependent transition peak position along ϵ traces out the energy dispersion of the hybridized eigenstates.

For increasing powers the possibility of multi-photon absorption and emission processes increases. They appear as additional resonance peaks parallel to the single photon

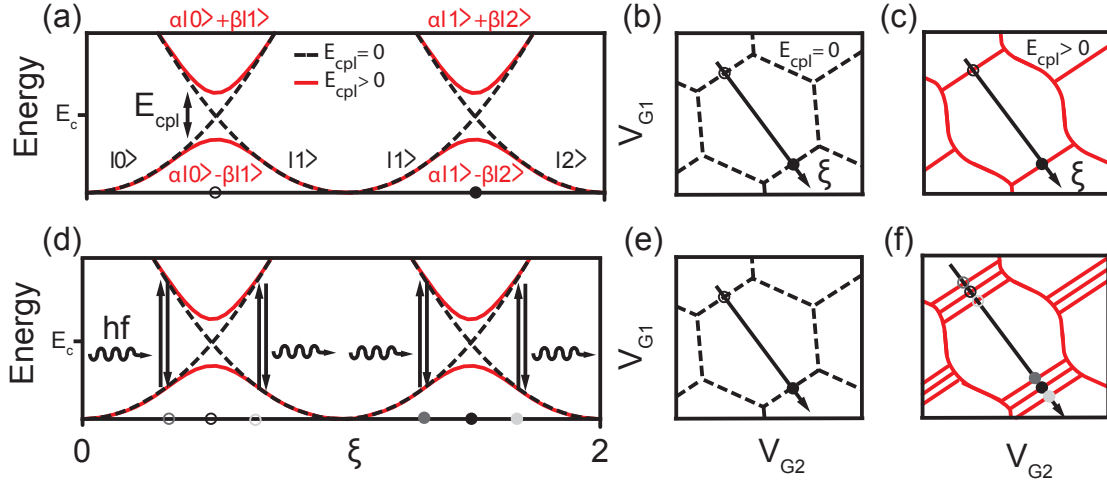


Figure 1.6: Mechanism of photon assisted tunneling in a tunnel-coupled double quantum dot: a) Energy dispersion of charge states as a function of the detuning axis ϵ . In the presence of a finite tunnel coupling energy ($E_{cpl} > 0$) the charge states $|0\rangle$ and $|1\rangle$ hybridize and anti-cross at degeneracy. b) Charge stability diagram indicating the charge state transitions in absence of a coupling energy ($E_{cpl} = 0$). c) Introducing the coupling energy $E_{cpl} > 0$ introduces anti-crossing reflected in the rounding of the hexagon outline. d) Microwave irradiation with frequency f leads to photon assisted tunneling between two charge states in coupled double quantum dots. e) Non-coupled quantum dots do not show signatures of photon assisted tunneling. f) Charge stability diagram of coupled double quantum dots shows resonant transition peaks parallel from the inter-island transition lines due to photon assisted tunneling.

one [36].

In this work, PAT is used to probe the coupling energy scales in a semiconducting-superconducting system with a mesoscopic double quantum dot geometry in the absence and presence of an external magnetic field (see Sec.1.4.4).

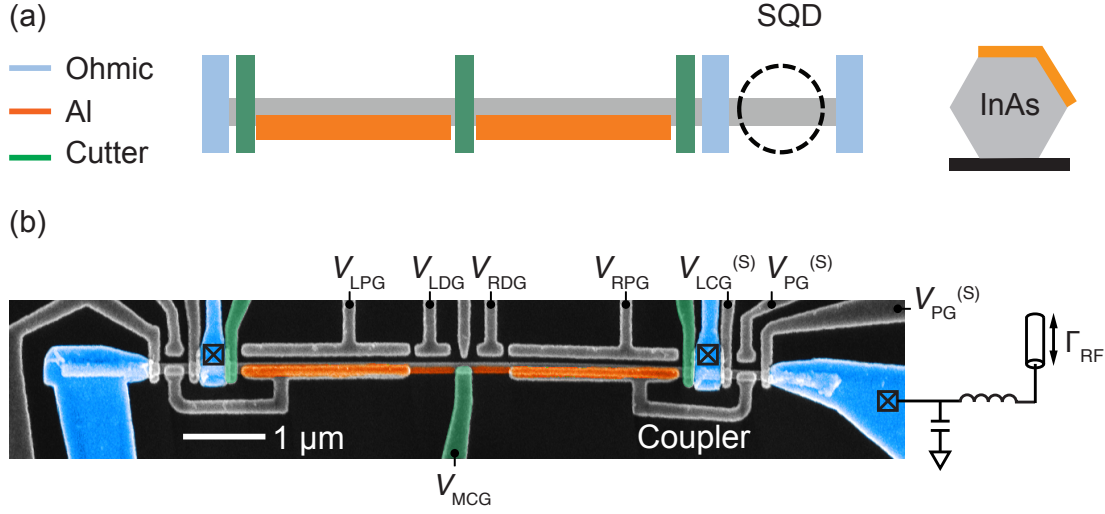


Figure 1.7: Mesoscopic double island geometry: a) Schematic representation of the investigated device: Ohmic contacts are represented in blue, the superconducting Al facets defining the two mesoscopic islands are highlighted in orange and cutter gates confining the double island are colored in green. A sensor quantum dot (SQD) residing on the same nanowire is used for charge state readout with a reflectometry circuit. The InAs nanowire has a hexagonal cross section with two facets covered with epitaxially grown Al. b) False colored scanning electron micrograph of the investigated hybrid double island device.

1.3 Materials and Methods

This chapter provides a brief overview of the investigated device geometry in Sec 1.3.0 and the fabrication procedure in Sec. 1.3.1. Further, the experimental set-up for low temperature quantum transport and sensing measurements will be introduced in Sec. 1.3.2.

1.3.0 Superconducting Double Island Device

The data presented in this thesis were measured on a single hybrid nanowire sample in a double quantum dot geometry (see Fig. 1.7 a, b). The two mesoscopic superconducting central segments, hereafter referred to as superconducting islands, are separated by a Josephson junction consisting of a bare semiconducting segment. The inter-island coupling is controlled by the tunneling barrier imposed by the middle cutter gate voltage (V_{MCG}). The device geometry is considered to be laterally symmetric with respect to the junction. Each island is equipped with a set of two electrostatic side gates,

here referred to as plunger ($\approx 2 \mu\text{m}$) and damper ($\approx 350 \text{ nm}$) gates. The plunger gate voltages (V_{LPG}, V_{RPG}) are used to define the electrostatic electron distribution inside the proximitized nanowire [21], [38]. The damper gate voltages (V_{LDG}, V_{RDG}) provide additional control over the coupling between energy states residing close to the tunnel barrier. Cutter gate voltages (V_{LCG}, V_{RCG}) between the superconducting islands and the inner ohmic contacts control the tunnel coupling of the respective island to the adjacent normal lead. This allows the system to transition between an open configuration for bias-spectroscopy characterization and a weak tunneling regime for charge sensing measurements.

Charge sensing is performed using a semiconducting sensor quantum dot (SQD) located at the right end of the nanowire (see Sec. 1.3.3.1). The SQD is created by introducing tunneling barriers *via* negative gate voltages on the left and right cutter gates ($V_{LCG}^{(S)}, V_{RCG}^{(S)}$). The sensor plunger gate voltage ($V_{PG}^{(S)}$) is used to tune the chemical potential of the SQD. The SQD is capacitively coupled to the superconducting islands *via* floating metallic U-shaped coupler segments (see Fig. 1.7 b). Like the gate electrodes, the couplers are separated from the nanowire by a dielectric layer. The device geometry has four ohmic contacts: The inner pair is used for two-probe quantum transport measurements with standard lock-in techniques (see Sec. 1.3.3.0) while the outer ones are connected to tank circuits for RF reflectometry readout of the charge state of the system (see Fig. 1.7).

1.3.1 Device Fabrication

1.3.1.0 Nanowires

The quasi one-dimensional super-semiconducting nanowires used for the device presented in this thesis were grown by Peter Krogstrup and his team at the *Center of Quantum Devices* using molecular beam epitaxy (MBE). The nanowires are grown using the bottom-up vapor-liquid-solid (VLS) technique facilitated by liquid gold (Au) particles that serve as collection centers for the indium (In) and arsenide (As) growth precursors [39]. The Au mediates the nucleation and growth of free-standing nanowires at the liquid-solid interface. The nanowires with wurzite crystal lattice possess hexagonal cross-sections with a diameter of approximately 100 nm. Subsequently, Aluminum (Al) is grown *in situ* on two of the facets of the nanowire with an epitaxially matched interface [40].

The nanowires are transferred on pre-patterned silicon (Si) blank substrates for further fabrication.

1.3.1.1 Device Fabrication

Devices are fabricated on a Si wafer with local Au backgates (for details, see Appendix A.0). To facilitate the deposition of the InAs nanowires onto the pre-patterned chip, they are broken off the growth substrate by stroking it with a cleanroom wipe. Nanowires lying on the substrate are picked up using an electrically grounded needle with a tip diameter of $0.1\ \mu\text{m}$ and deposited on top of the backgated area on the black substrate (see Fig. 1.8 a). The needle position is controlled using a semi-automated micro-manipulator setup. Steering the needle tip into close proximity of one nanowire end results in attracting Van-der-Waals forces causing one nanowire end to adhere to the needle which allows for the transport onto the chip. The subsequent deposition of the nanowires on the chip is done with an angular precision of $\approx \pm 5$ degrees.

Optical images and scanning electron micrographs containing pre-patterned alignment marks serve as references for drawing the top-down lithography masks using the *DesignCAD 23* software. Four different masks are designed: etching windows for selective removal of Al, ohmic contacts, windows for the growth of the dielectric, and gate electrodes (see Fig. 1.8 b-f).

A resist consisting of the organic molecule poly-methyl-methacrylate (PMMA) or shorter chains of its monomeric subunit MMA is spin-coated on the wafer to create the lithographically defined masks. Inside the *Elionix* electron beam lithography chamber, the masks are exposed with an accelerated electron beam (100 keV). The collisions between the electrons and the polymer molecules fragment the polymer chains in the exposed regions. In a subsequent step, the chip is submerged into a developer solution of N-methyl-2-pyrrolidone (MIBK) and isopropanol (IPA) at room temperature. This dissolves and washes out the exposed regions resulting in a negative mask of the designed pattern.

Al etching windows are selectively opened on the nanowire where the superconductor needs to be removed by the wet-etchant *Transene-D* at 50°C (see Fig. 1.8 b). Based on

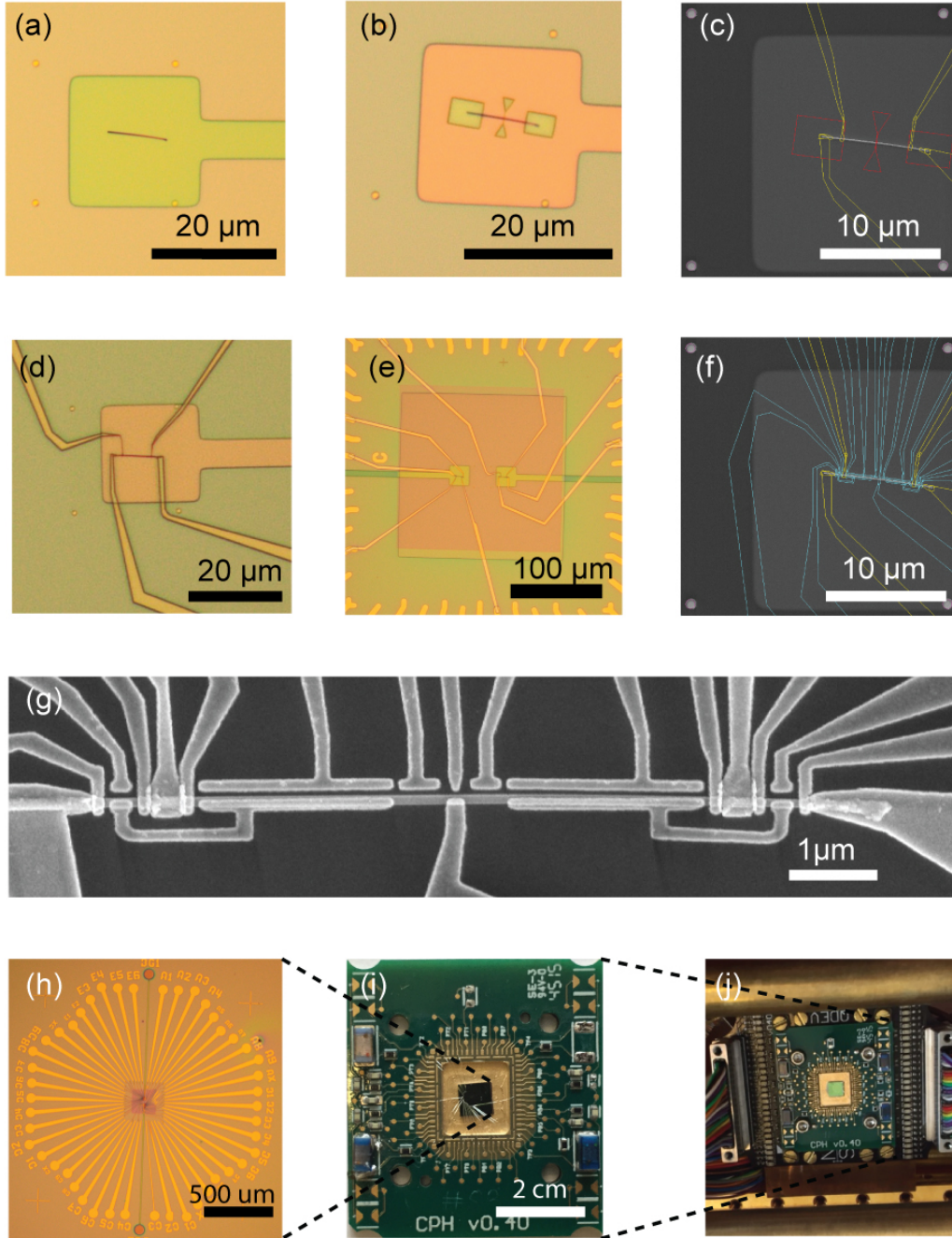


Figure 1.8: Fabrication procedure. a) Nanowire deposited onto the local backgate. b) Etching mask after development. c) Scanning electron micrograph of the nanowire overlaid with ohmic contact design (yellow) with reference to the preceding etching window (red). d) Optical micrograph of the device with ohmic contacts. e) Optical micrograph of device with evaporated Au ohmic contacts and dielectric layer of HfO_2 grown locally using atomic layer deposition. f) Scanning electron micrograph of the device overlaid with gate electrode design (blue). g) Scanning electron micrograph of the device after gate evaporation and lift-off. h) Overview of chip with meander structures ending in circular bonding pads. i) Chip bonded to daughterboard. j) Daughterboard loaded into motherboard inside the puck.

scanning-electron micrographs, a device is chosen with Al covering two facets opposite from the substrate-nanowire interface. This way, the back gate voltage V_{BG} can tune the density of states inside the nanowire without being screened by the Al. In the next step, the ohmic contacts are exposed and metalized (see Fig. 1.8 c, d). Radio frequency (RF) milling removes the native oxide layer covering the InAs nanowire to establish electrically conductive interfaces before introducing the vaporized metal. Titanium (Ti 5 nm) and Au (150 nm) are deposited. The Ti layer is added to ensure sufficient adhesion of Au to the device and substrate. The sample is submerged into 80° C warm NMP to remove the excess Au evaporated on top of the PMMA masks. Subsequently, the nanowire is capped with 7 nm of the dielectric hafnium dioxide (HfO_2) grown *via* atomic layer deposition (ALD) (see Fig. 1.8 e). Finally, gates are deposited (Ti 5 nm, Au 160 nm) using a rotating substrate holder under an angle to ensure continuous evaporation of the cutter gate electrodes and coupler segments partially covering the nanowire (see Fig. 1.8 g).

For a more detailed description of the fabrication procedure see Appendix A.

1.3.1.2 Configuring Sample for the Cryostat

The sample chip is glued to a daughterboard using silver paint. The connection between the device and the macroscopic measurement setup is established by Al wire bonds extending from the individual bonding pads located on the chip to a daughterboard (see Fig. 1.8 h, i). The daughterboard is mounted on a motherboard (see Fig. 1.8 j). Electrical connection between the daughterboard and the motherboard located inside the puck is established *via* an interposer and fuzz buttons that lead to the lines inside the cryostat.

1.3.2 Measurement Setup

The sample located inside a puck is loaded into a dilution refrigerator and connected to a set of measurement equipment both for DC transport and high frequency experiments.

1.3.2.0 Dilution Refrigerator

To observe quantum mechanical phenomena the device has to be cooled down to low temperatures. The critical temperature for Al to transition from the metallic to the

superconducting phase is around 1.2 K. Furthermore, the thermal energy has to be small in comparison to the other energy scales present in the system to minimize thermal broadening.

Therefore, measurements were conducted in a cryo-free *Triton Cryofree* dilution refrigerator with a base temperature of ≈ 15 mK. This temperature is accessible due to the unique properties of a liquid ^4He - ^3He mixture [41] and advanced system engineering. The cryostat is compartmentalized into sub-chambers of decreasing temperatures: The 4K stage (4 K), still stage (1 K), cold plate (0.1 K) and finally the mixing chamber (0.02 K) where the sample is located (see Fig. 1.9). Pulse tubes relying on heat exchangers are employed to cool down the sample to cryogenic temperatures.

The cryostat is equipped with a three-axis (1-1-6) T superconducting vector magnet. The loaded device is roughly aligned with the z axis. This alignment can be fine-tuned by rotating the magnetic field (see Sec. 1.11).

1.3.3 Measurement Techniques

Both DC transport and charge sensing measurements with frequencies up to GHz are conducted. The sample inside the cryostat is connected to the measurement equipment *via* coaxial cables of different bandwidths. SMP coaxial lines are used for high frequency (HF) signals while BNC coaxial cables transmitted low frequency and DC inputs. Detailed schematics of the cryostat configuration and equipment setup are depicted in Fig. 1.9.

1.3.3.0 Quantum Transport Measurements: Lock-in Amplifier

Transport measurements were conducted in a two terminal setup using standard Lock-in techniques with a *Stanford Research Systems SR830 DSP* amplifier. An AC voltage excitation frequency and DC bias voltage enter over an in-house build voltage divider and are applied to the sourcing ohmic contact. The voltage divider reduces the AC amplitude by a factor of 10^{-5} and for the DC voltage signal by 10^{-3} . For the measurements presented in this thesis the AC amplitude is around $10 \mu\text{eV}$ at a frequency of approximately 130 Hz. The current response to the source-drain voltage bias is measured *via* the drain electrode and converted to a voltage signal using a *Basel* transimpedance amplifier with

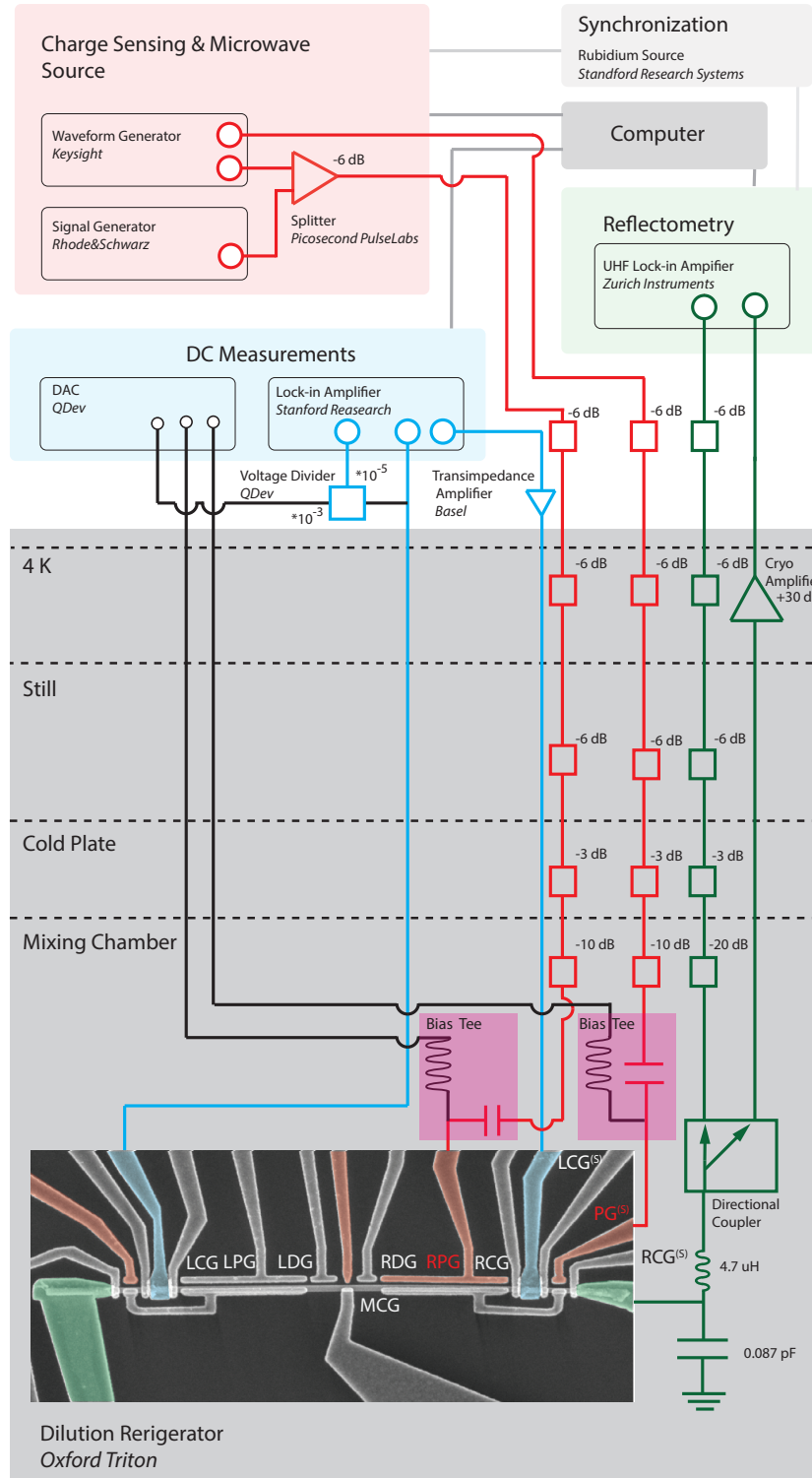


Figure 1.9: Schematic representation of the measurement setup of equipment and configuration of the cryostat including a false colored scanning electron micrograph of the device. Ohmic contacts and the connecting cables are represented in blue, green denotes RF reflectometry lines, red represents gates addressed via high frequency coaxial lines and non-colored gray electrodes all represent gates connected to the DAC via BNC coaxial cables.

an I/V gain of 10^7 .

Homodyne detection is performed in the Lock-in amplifier by mixing, filtering and amplifying the signal at room temperature. Digital division of the measured current by the applied AC excitation amplitude gives the differential conductance dI/dV which is converted into units of the conductance quantum $2e^2/h$, where h is Planck's constant. All DC signals applied to the gate electrodes and ohmic contacts addressed by low frequency lines are generated using a digital-to-analogue converter (DAC).

The conductance value in the presented transport data includes the line resistance of $\approx 0.8 \text{ k}\Omega$.

1.3.3.1 Fast Charge Sensing with Reflectometry

The charge states of the superconducting double island are investigated using fast charge sensing with reflectometry readout. The gate voltages serving as the axes of corresponding charge stability diagrams (see Sec. 1.2.9) are swept using techniques associated with different speeds of data acquisition. In laboratory jargon they are referred to as fast and slow axis. The fast axis voltage is swept by adding a continuous saw-tooth ramp pulse with a frequency of 2.8 kHz from a *Keysight 33500B* waveform generator on top of the DC signal in a bias tee located on the motherboard (see Fig. 1.9). For the presented data the fast axis always corresponds to the right island plunger gate voltage (V_{RPG}) since it is connected to a HF line. After every ramp cycle the voltage of the slow gate axis is stepped using the DAC.

Charging events of the double island induced by the nearby gate electrodes are simultaneously read-out using reflectometry on the capacitively coupled right SQD (see Sec. 1.7).

Reflectometry is a measurement technique used to non-invasively probe a load resistance. It is based on the principle of impedance-match dependent reflection of periodic electromagnetic waves at circuit interfaces.

An input sinusoidal radio frequency (RF) electromagnetic wave is generated by a *Zurich Instruments Ultra High frequencies Lock-in* waveform generator (UHFLI) and

propagates through an SMP coaxial cable. The transmission line has a characteristic impedance of $Z_0 = 50 \Omega$. The line is terminated by a RLC-circuit, referred to as a tank circuit, composed of a resistive element (R), an inductor (L) and a capacitor (C) [42].

The amplitude of the reflected signal depends on the transmission line impedance Z_0 and the impedance of the tank circuit load Z_L . The reflection coefficient τ is given by:

$$\tau = \frac{Z_L - Z_0}{Z_L + Z_0}, \quad (1.17)$$

where Z_L is a function of L, C, R and the frequency f . Based on preliminary optimization experiments, an inductor with $L = 4.7 \mu\text{H}$ was chosen and soldered onto the daughterboard. The capacitance C is determined by the parasitic capacitance of the environment. The resistance R of the tank circuit is indirectly probed through the conductance of the SQD which varies with its electrostatic environment. The value of τ in Eq. 1.17 goes to zero when $Z_L = Z_0$, which corresponds to the total absorption of the RF signal by the load. The condition of total reflection is only fulfilled for the resonance frequency of the tank circuit f_R where the system is most sensitive to changes in resistance. The resonance frequency depends on L and C as:

$$f_R \approx \frac{1}{2\pi\sqrt{LC}}. \quad (1.18)$$

Based on frequency sweeps as a function of the reflection coefficient f_R was determined to be 248 MHz. This gives $C = 0.087 \text{ pF}$.

The high frequencies applicable for reflectometry result in an effectively small $1/f$ noise contribution and large bandwidth. A further motivation to use reflectometry in combination with fast gating is the increased speed of data acquisition compared to standard lock-in measurements [43].

RF reflectometry readout is implemented by employing a series of circuit elements [44]. The input RF excitation propagates through a coaxial cable and gets divided by a power splitter. Part of the signal is used as a reference for homodyne detection by getting mixed with the reflected signal and demodulated using a low pass filter and amplifier. The other part of the signal is attenuated inside the cryostat (-41 dB) and enters a three port directional coupler located in the mixing chamber getting reflected at the the tank

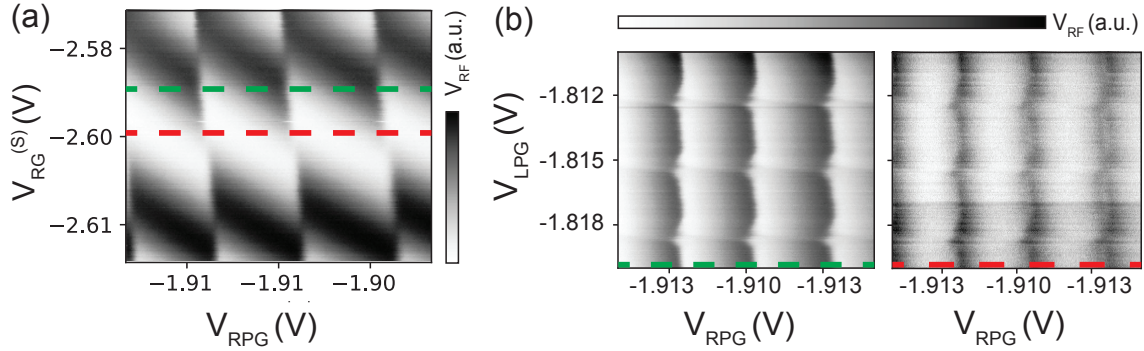


Figure 1.10: Charge sensing optimization at $B=0$: a) Reflectometry signal as a function of the right island plunger voltage V_{RPG} and the sensor plunger gate $V_{PG}^{(S)}$. The horizontal sawtooth pattern shows Coulomb blockade on the right island. The vertical black-white-black transition corresponds to crossing one Coulomb blockade peak on the sensor quantum dot. b) Charge stability diagram obtained for optimized (left panel) and unoptimized position (right panel) of $V_{PG}^{(S)}$.

circuit interface. The reflected signal is amplified using a Cryo amplifier at 4 K before entering the UHFLI.

To optimize the system for reflectometry readout the sensor plunger gate voltage ($V_{PG}^{(S)}$) is used to tune the SQD into the linear regime of its Coulomb peak slope. There, the readout is most sensitive to changes in conductance (see Fig. 1.10 a, b left panel). For $V_{PG}^{(S)}$ values off the linear regime the sensing resolution gets compromised (see Fig. 1.10 b right panel).

Variations in the electron distribution of the environment induce small shifts in the Coulomb peaks resulting in changes in the resistance value of the SQD.

Reflectometry reads out resistance changes of the SQD - since they reflect the charging and discharging events occurring on the double-island.

An artifact which requires compensation is the capacitive coupling between the sensor dot plunger gate ($PG^{(S)}$) and the RPG. When charge sensing data are obtained by ramping V_{RPG} , the fast gating of the RPG introduces a shift of the sensor QD levels independent of double-island charging events. This coupling is compensated by using the second channel of the *Keysight 33500B* to stay in the linear regime. The compensation is chosen to highlight the charge state transitions rather than assigning a homogeneous

reflection coefficient value to the individual charge states. This, however, is purely an effect of the compensation scheme and contains no additional physical meaning.

All charge sensing data presented in this thesis are taken at effectively zero bias.

1.3.3.2 Continuous Microwaves

Microwaves are applied to the RPG using a *Rohde&Schwarz S100A* signal generator. The GHz signal is added on top of the 2.8 kHz sawtooth voltage profile of the RPG. The power has to be optimized for the different frequencies to ensure that the signal reaches the sample despite resonances introduced by the setup. All HF instruments are synchronized using a *Stanford Research system FS725* rubidium source operated at 10 MHz.

1.4 Results and Discussion

The motivation of this experiment was to coherently probe the coupling between two Majorana bound states across a controllable junction. There were primarily three energy scales of interest. Firstly, the Josephson energy E_J arising from Cooper pair tunneling. Secondly, the single electron coupling strength E_{1e} and finally, the charging energy E_C , which is relevant, since its relationship with E_J determines the degree of charge dispersion in the system [45].

The superconducting double island device introduced in Sec. 1.3.0 was investigated in transport and charge sensing. In Sec. 1.4.0 and Sec. 1.4.1, the optimization of the magnetic field orientation and an initial device characterization are shown. Subsequently, transport data of a zero bias conductance peak at 750 mT and its magnetic field evolution are presented in Sec. 1.4.2. Sec. 1.4.3 discusses the transition of the Coulomb blockaded double island from a $2e$ to a $1e$ periodic ground state with magnetic field. Finally, microwave spectroscopy data are presented for $B = 0$ in Sec. 1.4.5 and $B = 750$ mT in Sec. 1.4.6 providing estimates of E_J , E_{1e} and E_C .

1.4.0 Aligning the Magnetic Field along the Nanowire

Superconductivity as well as a finite axial magnetic field are essential criteria for the emergence of MBSs (see Sec. 1.2.4). While the magnetic field can transition the superconductor into the topological regime, it can also destroy superconductivity when a critical magnetic field B_C is exceeded. Their co-existence can only yield MBSs when $B_C > B > \frac{\sqrt{\mu^2 + \Delta^2}}{\mu_B g}$ (see Sec. 1.2.4).

Superconducting bulk material expels magnetic flux below a characteristic London penetration depth λ by means of a screening supercurrent. This phenomenon is known as the Meissner effect. A penetrating magnetic field H decays exponentially with increasing distance x from the surface of the superconductor [17]:

$$H(x) = H(0)e^{-\frac{x}{\lambda}} \quad (1.19)$$

Therefore, the size of the proximity-induced superconducting gap in the hybrid nanowire depends strongly on the alignment of the external magnetic field with respect to its two aluminum facets.

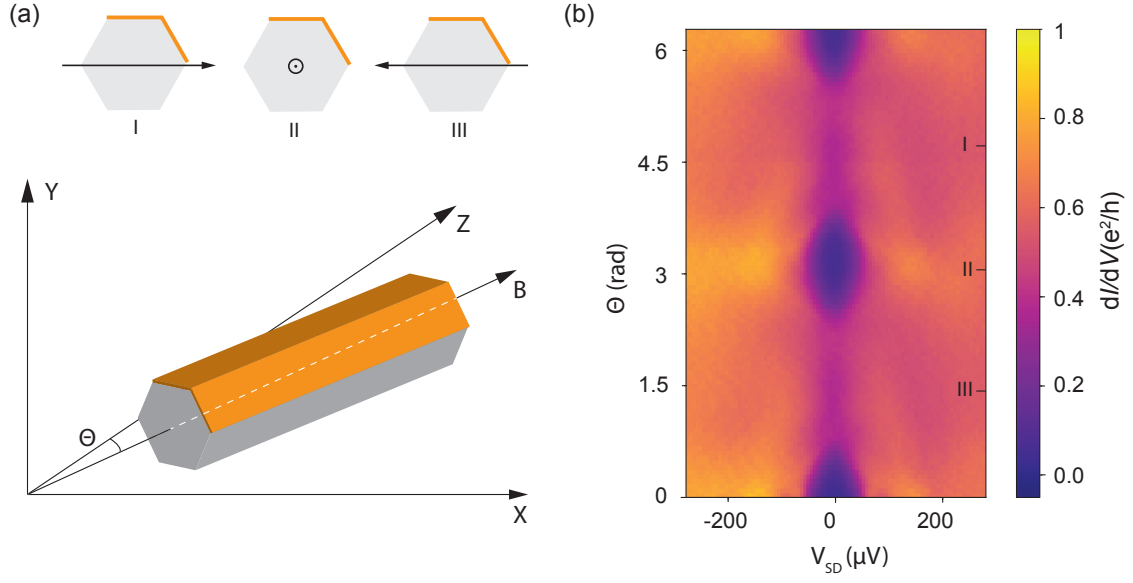


Figure 1.11: Magnetic field alignment to the nanowire orientation: a) Schematic representation of the alignment of the effective magnetic field B of the 3-vector magnet to the nanowire. b) Differential conductance dI/dV at a function of source drain bias V_{SD} and the magnetic field rotation angle Θ .

The manual alignment of the nanowire on the substrate with the micromanipulator during the fabrication process is only precise within approximately ± 5 radial degrees (see Sec. 1.8). The effective magnetic field B resulting from the 3-axis vector magnet has to be aligned with the orientation of the quasi-one-dimensional nanowire as an initial configuration step to maximize B_c . Rotating the magnetic field axis in the x - z substrate plane through the angle Θ and looking at the superconducting gap in source-drain bias spectroscopy reveals an angle-dependent superconducting gap Δ (see Fig. 1.11 a, b). When the external field is perpendicular to the Al-coated nanowire, superconductivity is maximally suppressed ($\approx \Theta_{1,2} = 1.5, 4.7$ rad). For magnetic field orientations parallel to the direction of the nanowire the superconducting gap size is maximized ($\approx \Theta_{3,4} = 3.1, 6.2$ rad). Experiments at finite field were conducted at $\Theta_{3,4} = 3.144$ rad.

1.4.1 Initial Characterization

To characterize the transmission controllability of the cutter gates defining the double island (LCG, MCG, RCG), their pinch-off curves were taken (see Fig. 1.12 a-c). A trans-

mission barrier got introduced under increasingly negative gate voltages applied to cutter gates individually, which eventually fully suppressed conductance through the nanowire.

All pinch-off curves reveal several conductance resonances. They presumably arise either from quantum dots introduced to the system during the device fabrication or are standing waves due to disorder and confinement in the semiconductor crystal. The Al etching step is assumed to cause perturbations in the potential landscape of the nanowire. The control over the wet etching process is limited. During the empirically optimized etching time, the etchant was seen to not only remove the Al but also to attack the InAs and its native oxide layer at different rates. This roughens the surface of the nanowire, giving rise to an inhomogeneous potential landscape, which presumably contributes to the observed resonances in the pinch-off curves. Resonances can also be caused by impurities on the nanowire surface. These can be microscopic Al residues or they can be introduced by the atmospheric environment during the fabrication process. Resonances in the MCG pinch-off trace can cause large changes in the inter-island transmission within small V_{MCG} intervals. Throughout the experiment the system was tuned in a V_{MCG} -regime which minimized resonance effects in order to have consistent transmission control.

Comparing the opening and closing traces of the tunnel barriers further reveals hysteresis. Measurements were performed with static cutter gates, making the effect of hysteresis insignificant. For qubit protocols involving cutter gate pulses the observed hysteresis would, however, impose a relevant obstacle.

1.4.2 Hunting in Bias Spectroscopy

In contrast to most of the previous experimental work investigating MBSs signatures in tunneling bias spectroscopy using a normal lead [3], [5], [6], the system was probed in a semiconductor-insulator-semiconductor (S-I-S) configuration. The Josephson junction, controlled by V_{MCG} , imposed a transmission barrier between the two superconducting islands while positive V_{LCG} , V_{LCG} values allowed for transport between the islands and leads.

Tunneling bias spectroscopy was used to indirectly probe the local density of states at

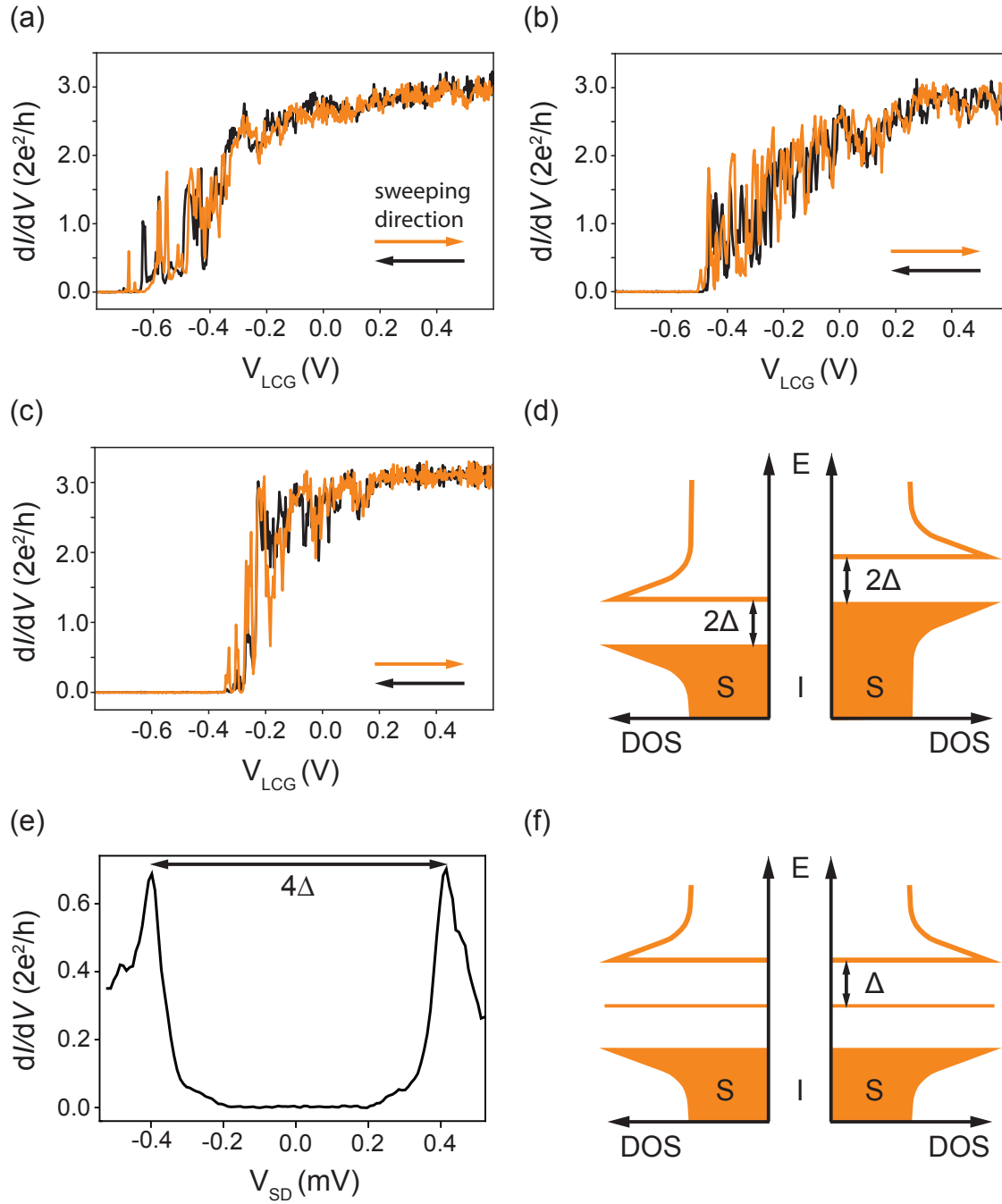


Figure 1.12: Initial characterization: Pinch-off curves with cutter gate voltages of opening (orange) and closing (black) traces with a) left cutter gate V_{LCG} . b) right cutter gate V_{RCG} . c) middle gate V_{MCG} . d) Schematic representation of density of states in a superconducting(S)-insulating(I)-superconducting configuration. e) Differential conductance dI/dV as a function of source drain voltage V_{SD} in a S-I-S configuration revealing the superconducting gap Δ . f) Schematic representation of density of states in a S-I-S configuration in the presence of two zero energy states.

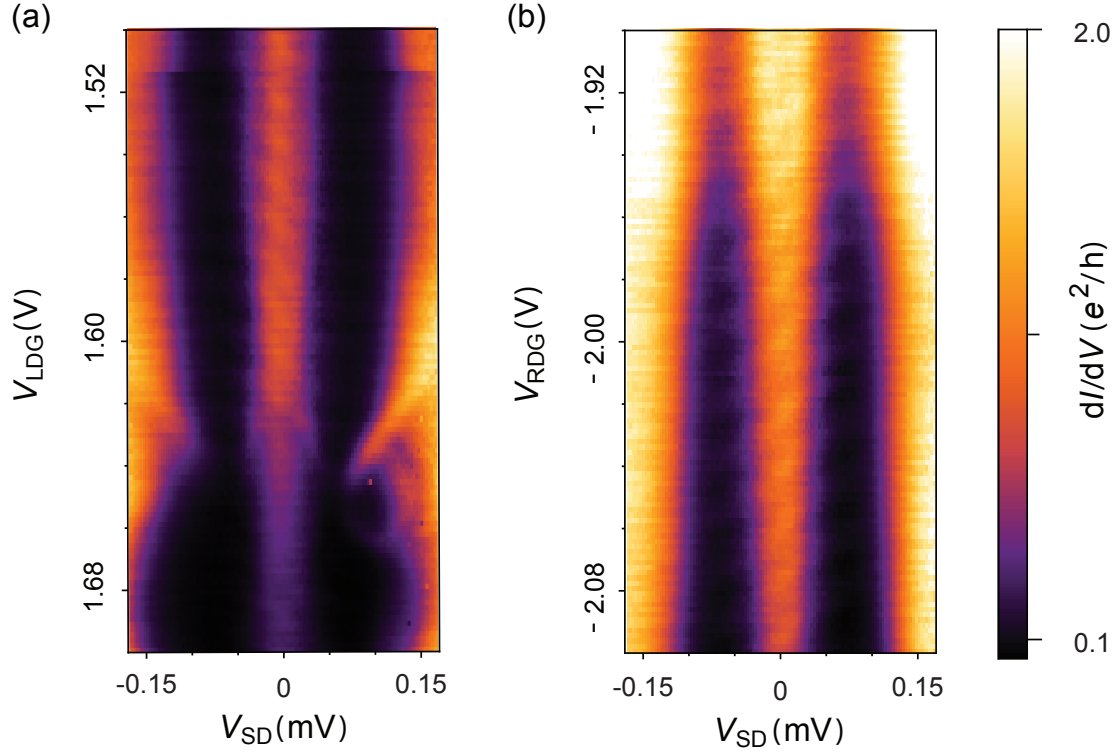


Figure 1.13: Gate stability of zero bias conductance peak in S-I-S tunneling bias spectroscopy at 750 mT: Differential conductance dI/dV as a function of source-drain bias V_{SD} and a) left damper gate voltage V_{LDG} . b) right damper gate voltage V_{RDG} .

the Josephson junction [22]. In an S-I-S configuration the measured superconducting gap between the two coherence peaks corresponds to 4Δ . Single electron tunneling events can only occur when the electron continuum is aligned with the energetically accessible hole states in the quasiparticle continuum of the respective other superconductor (see Fig. 1.12 d).

The proximity effect in the hybrid system was verified by measuring the differential conduction as a function of source-drain bias voltage V_{SD} in an S-I-S configuration. Fig. 1.12 e demonstrates the characteristic density of states of a superconductor with an energy gap $\Delta \approx 200 \mu\text{V}$. This confirms the proximity induced superconductivity in the InAs nanowire.

This work is motivated by probing the cross-junction coupling of two Majorana bound states which are predicted to emerge at finite magnetic field and would manifest themselves as a mid gap peak in S-I-S (see Fig. 1.12 f). Therefore, the hunt – as it is referred

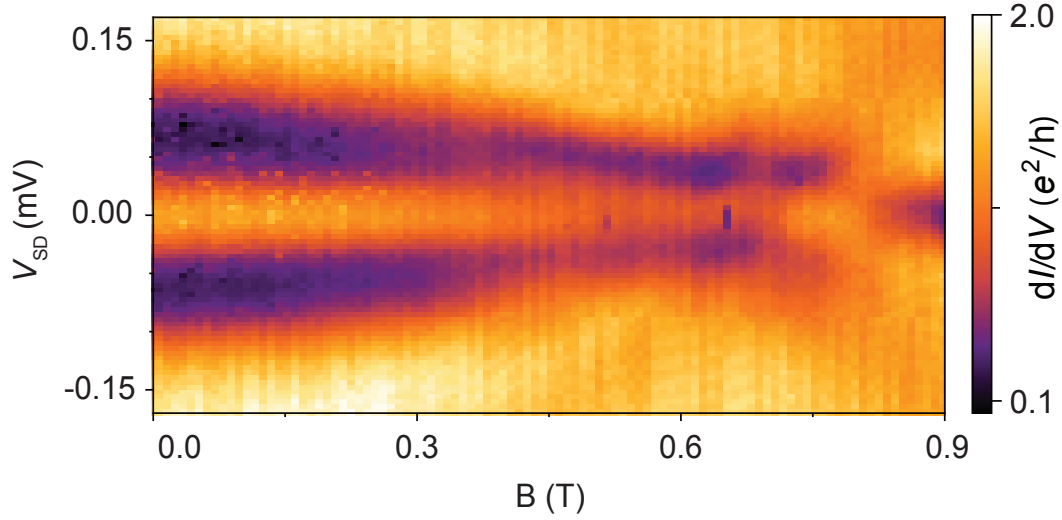


Figure 1.14: Magnetic field evolution: Differential conductance dI/dV as a function of source drain bias voltage V_{SD} and axial magnetic field B .

to in jargon – for these exotic states was conducted at 750 mT. A ZBP demonstrating stability over more than 100 mV in damper gate voltages is presented in Fig. 1.13 a, b. The tunneling bias spectroscopy data further demonstrate that at 750 mT the ZBP is separated from the quasiparticle continuum by a superconducting energy gap of $\Delta \approx 75 \mu\text{V}$.

Different physical origins could explain of the observed ZBP at finite magnetic field. As mentioned, zero energy states on both sides of the junction, would give rise to a midgap conductance peak in S-I-S. These states could be MBSs or trivial ABSs which can give rise to the same transport characteristics as discussed in Sec. 1.2.4. Further, since the mesoscopic double island system is effectively a Cooper pair box, a Josephson coupling $E_J \cos(\Phi)$ could give rise to a supercurrent driven by the difference in superconducting phase Φ between the two islands [17]. This process, which is mediated by Andreev reflections (see Sec. 1.2.5), can result in a ZBP. The charge of supercurrent is quantized in units of $2e$ and the ZBP can persist from high magnetic fields down to $B = 0$ in contrast to ABSs and MBSs, which are restricted to finite magnetic fields and allow for single electron population of the hybrid double island.

Fig. 1.14 shows the magnetic field dependence of the ZBP (taken at $V_{LDG} = -1.609 \text{ V}$ and $V_{RDG} = -1.984 \text{ V}$) as a function of the source drain bias V_{SD} . The relatively transparent Josephson junction ($V_{MCG} = -0.109 \text{ V}$) results in limited spectral resolution of

quantum transport. The soft gap presumably arises due to multiple Andreev reflections. The ZBP as a dominant feature can still be resolved, persisting for magnetic fields from 0 T all the way to 0.8 T where the ZBP splits. The difference to the hard superconducting gap with $\Delta = 200 \mu\text{V}$ presented in Fig. 1.12 e is believed to mainly arise from a difference in the back gate voltage V_{BG} . Fig. 1.12 e was taken at $V_{BG} = -2.21 \text{ V}$, which pushes the electrons in the nanowire away from the substrate interface towards the Al shell [21], [38]. Increasingly negative values of V_{BG} deplete the nanowire and pinch off conductance through the semiconductor. All data presented besides Fig. 1.12 e, however, were measured at $V_{BG} = 0$ associated with a softer gap which was motivated by the expectation of stronger inter-island coupling.

Based on transport data alone it is difficult to distinguish whether the ZBP measured at 750 mT originates from the same physical phenomenon as the one at zero magnetic field. It is only in charge sensing where intriguing additional information is obtained, indicative of the emergence of discrete zero energy bound states at finite magnetic field.

1.4.3 Magnetic Field Evolution in Charge Sensing

In addition to the presented quantum transport data the charge states of the device in single- and double-island configuration were measured in fast charge sensing using a RF reflectometry circuit for readout (see Sec. 1.3.3.1). The cutter gate voltages V_{MCG} , V_{RCG} put the right island in a weak tunneling regime where the charging energy E_C fixed the total charge. Fig. 1.15 a shows the transition from a 2e to a 1e periodic ground state with magnetic field via an intermediate even-odd regime for the Coulomb blockaded right superconducting island.

The double island – established by also putting the left island into a weak tunneling regime using V_{LCG} – also shows an analogous 2e to 1e transition with magnetic field in charge stability diagrams (see Fig. 1.15 b).

There are several physical phenomena that can give rise to the observed periodicity change. For one, the superconducting-normal phase transition occurring at B_C allows for the emergence of 1e transport with increasing B . For low values of B and $E_C < \Delta$ only CPs are allowed to tunnel onto the superconducting island. Due to their effective bosonic properties CPs can populate the Bose-Einstein condensate pinned to the middle of the

proximity induced energy gap. Corresponding Coulomb blockade shows $2e$ periodicity. Single electron tunneling events are allowed as soon as Δ descends below E_C . While the charge on the mesoscopic double island in that configuration would correspond to an integer multiple of $1e$, the charge state degeneracy spacing would demonstrate even-odd behavior and would only become $1e$ periodic at $B = B_C$. Fig. 1.15, however, demonstrates the transition to $1e$ periodic transitions takes place at approximately 600 mT while the investigated system was seen to maintain a superconducting gap up to at least 1200 mT. This excludes $E_C > \Delta$ as well as a normal state origin as a potential source of the single electron tunneling events.

The periodicity between charge transitions observed in Fig. 1.15 doubles *via* an even-odd splitting starting at approximately 300 mT. This indicates that the $1e$ periodicity at finite magnetic field does not arise from quasiparticle poisoning [46] but from a discrete state lowering its zero-point energy for increasing Zeeman fields [47]. The emergence of both ABSs and MBSs are consistent with the presented Coulomb blockaded charge sensing data.

In order to further confirm that the ZBP at 750 mT emerges from bound states residing on both sides of the Josephson junction, the presence of a cross-junction coupling was investigated by photon assisted tunneling (PAT, see Sec. 1.2.10). A normal state origin ($B > B_C$) of the $1e$ periodic Coulomb blockade is not expected to give rise to any detectable response to microwave excitation due to the lack of resolvable level spacing in mesoscopic semiconducting island. since anti-crossings in a continuum are not resolvable.

1.4.4 Photon Assisted Tunneling

The previously discussed ZBP measured in transport (see Sec. 1.4.2) was investigated using microwave spectroscopy in charge sensing in the absence and presence ($B = 750$ mT) of an external axial magnetic field. The system was in the same gate configuration as in Fig. 1.14 with the exception of the left and right cutter gate voltages (V_{LCG} and V_{RCG}) used to impose tunneling barriers to discretize the number of charge carriers on the islands due to Coulomb blockade for charge state readout.

The Hamiltonian H describing the mesoscopic double island hybrid system consists

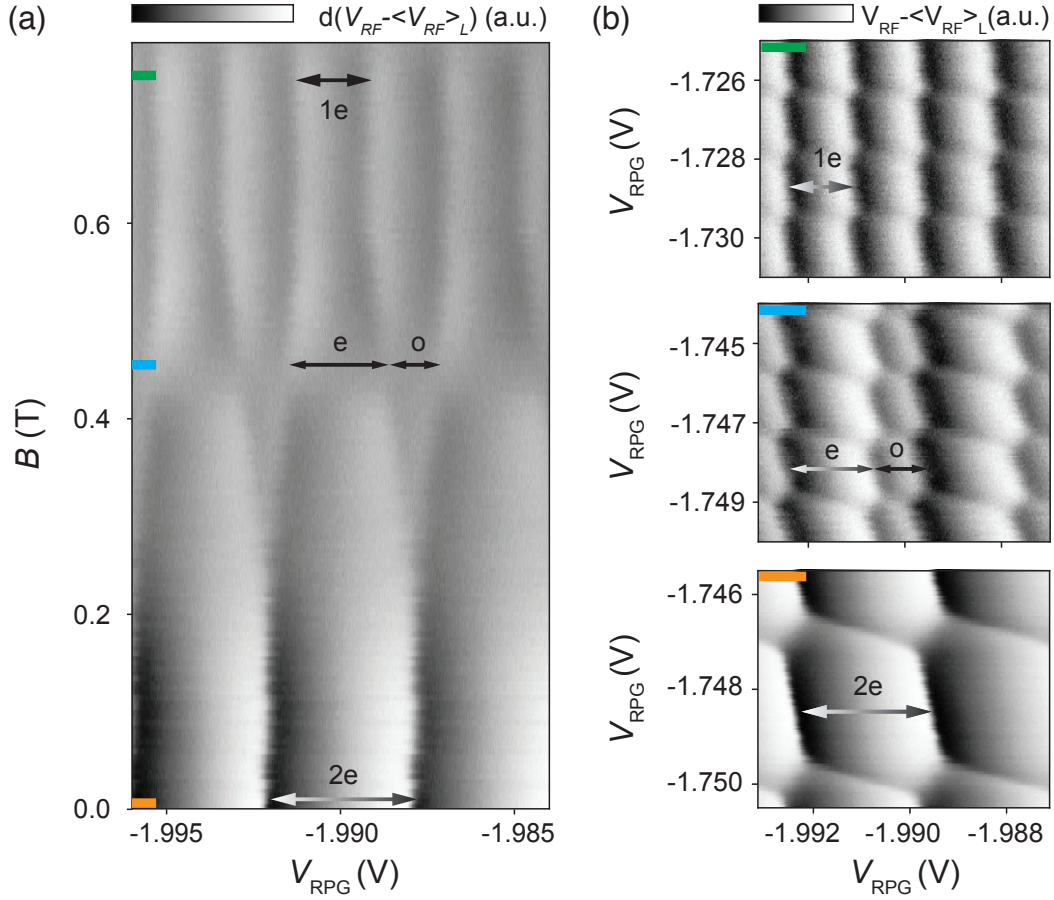


Figure 1.15: $2e$ to $1e$ Coulomb peak periodicity change in magnetic field *via* an even (e) and odd (o) regime: a) Magnetic field evolution of the right superconducting island in charge sensing as a function of the right plunger gate voltage V_{RPG} . b) Charge stability diagrams of Coulomb blocked double island for 750 mT (upper panel), 450 mT (middle panel), 0 mT (lower panel) showing the transition from a $2e$ to a $1e$ periodic system *via* an even-odd regime.

of three significant terms accounting for the charging energy, the superconducting contribution and the inter-island tunnel coupling [48]:

$$H = H_C + H_{SC} + H_t. \quad (1.20)$$

H_C includes the charging energy of both islands (E_{C_L}, E_{C_R}) as well as the inter-island mutual charging energy E_{CM} . The superconducting term H_{SC} accounts for the energy penalty of hosting an unpaired electron on the double quantum dot denoted by E_{SC} . The tunneling term H_t includes single electron as well as Cooper pair tunneling between

the two islands across the Josephson junction, which induces the inter-island coupling. The Josephson coupling is given by E_J . Due to the unambiguous nature of bound states associated with the $1e$ periodicity at finite field the single electron coupling energy is denoted by E_{1e} . The three individual Hamiltonian terms can be expressed for the charge carrier occupation number on the left and right islands N_L , N_R , the gate induced charge on the islands N_{gL} , N_{gR} and the superconducting phase difference between the two islands $\Delta\Phi = \Phi_L - \Phi_R$ [48]:

$$H_C = E_{CL}(N_L - N_{gL})^2 + E_{CR}(N_R - N_{gR})^2 + E_{CM}N_LN_R \quad (1.21)$$

$$H_{SC} = E_{SC_L} \frac{1}{2}[1 - (-1)^{N_L}] + E_{SC_R} \frac{1}{2}[1 - (-1)^{N_R}] \quad (1.22)$$

$$\begin{aligned} H_t &= E_J \cos(\Delta\Phi) + E_{1e} \cos\left(\frac{\Delta\Phi}{2}\right) \\ &= \frac{1}{2}E_J(|N_L + 2, N_R - 2\rangle \langle N_L, N_R| + h.c.) \\ &\quad + \frac{1}{2}E_{1e}(|N_L + 1, N_R - 1\rangle \langle N_L, N_R| + h.c.) \end{aligned} \quad (1.23)$$

Measurements were conducted in a Coulomb blockaded configuration, where the total charging energy $E_C = E_{CL} + E_{CR} - E_{CM}$ fixes the total charge of the double island $N = N_L + N_R$. The system can therefore be expressed in the basis of N and the difference in charge between the two islands $N_- = N_L - N_R$. Since N remains constant for equi-charge states, which this work is focused on, the state notation can be reduced to $|N_- \rangle$.

The tunnel-coupled system described by Eq. 1.20 gives rise to symmetric and antisymmetric hybridized eigenstates which are superpositions of the original states. The hybridization induces an anti-crossing opening up a coupling energy-dependent energy gap at charge state degeneracy (see Sec. 1.2.10). The inter-island coupling can be controlled by V_{MCG} (see Fig. 1.16 a-c). By controlling the tunnel coupling, the system can be transitioned from localized to delocalized charge states [36]. PAT was used as a spectroscopic tool to map the energy dispersion of the hybridized eigenstates both in the presence and absence of an external magnetic field. This provides an estimate for the respective coupling energies E_J and E_{1e} .

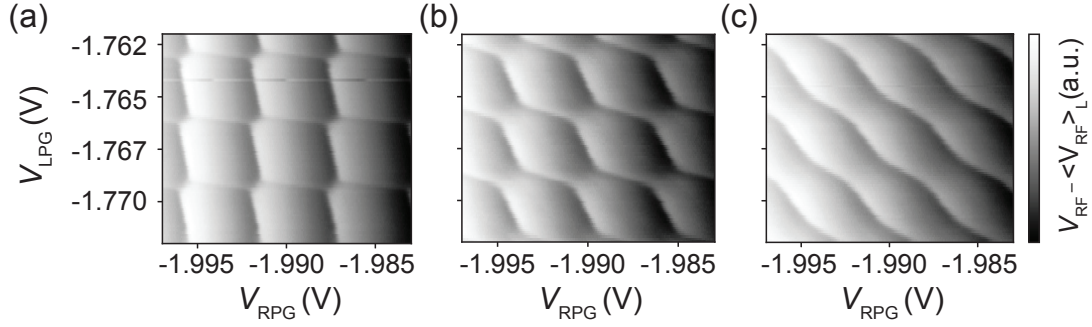


Figure 1.16: Middle cutter gate voltage V_{MCG} controlled coupling between two mesoscopic superconducting double islands in charge sensing: a) Weakly coupled regime ($V_{MCG} = -82.6$ mV). b) Intermediate coupling regime ($V_{MCG} = -71.0$ mV). c) Strongly coupled regime ($V_{MCG} = -64.2$ mV).

To induce inelastic photon assisted tunneling, a time-dependent oscillating excitation potential with frequencies f on the order of GHz was applied to the RPG (see Sec 1.3.3.2). Photon absorption and emission takes place at resonance when the photonic excitation energy – given by Plack’s law $E = hf$ – corresponds to the energy difference between the hybridized eigenstates. This enables inelastic tunneling of electrons (or CPs for $2e$ periodic systems) delocalizing the two charge state eigenfunctions across the double dot system [37].

Extracting the coupling energy is an important step for the coherent manipulation of two quantum states in a qubit. The coupling energy determines the frequency required to coherently drive the system at the charge state degeneracy point [49].

Nakamura *et. al.* first demonstrated charge coherence in a Cooper pair box [27] by controlling the coupling with gate pulses. Charge qubits based on similar operating schemes have also been implemented in semiconducting double quantum dot geometries [50], [51], [52].

If the investigated hybrid system were to transition into the topological phase, four Majorana bound states ($\gamma_1, \gamma_2, \gamma_3, \gamma_4$) would nucleate at the boundaries between the topological superconductor and the trivial phase (see Fig. 1.17). This work is focused on trying to probe the Majorana coupling E_M between γ_2 and γ_3 across the Josephson junction. Depending on the transmission set by V_{MCG} , the two MBSs could hybridize by means of wavefunction overlap, creating a coherent superposition of the two exotic

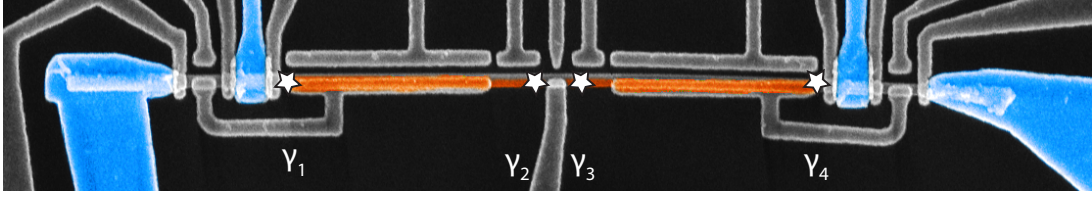


Figure 1.17: Scanning electron micrograph of the device indicating the theoretically predicted positions where Majorana bound states $\gamma_{1,2,3,4}$ (represented by stars) would nucleate in the topological phase.

states. The induced eigenenergy splitting would correspond to E_M at charge degeneracy.

The introduced mesoscopic double island hybrid system in the presence of an external magnetic field theoretically provides a platform for a Majorana-based charge qubit. While the charge qubit protocol would not allow for topological protection and the nanowire platform is not scalable, it would mark a milestone as a proof-of-principle Majorana bound state qubit on the journey towards topological quantum computing.

As a starting point, photon assisted tunneling of CPs in the absence of an external magnetic field will be presented which has been observed in a superconducting Cooper pair box [53] but has never been reported for a superconducting-semiconducting hybrid system.

1.4.5 Photon Assisted Tunneling in Absence of an External Magnetic field.

The previously discussed magnetic field evolution in bias spectroscopy (see Fig. 1.14) shows a ZBP already at $B=0$.

Protected by charging energy and the superconducting gap, excitations were shown to only occur between $2e$ periodic ground states (see Fig. 1.15). Coherent tunneling events across the Josephson junction are mediated by CPs giving rise to a Josephson exchange energy E_J [54], [55]. The corresponding conductance peak at zero bias in transport is therefore interpreted as supercurrent.

A detuning axis ϵ was defined in In Sec. 1.2.9 marking a trajectory in charge stability

diagrams along which the system transitions between equi-charge states. Hereafter, a normalized detuning axis denoted by n_g is used for which any two neighboring inter-island charge state transitions are separated by $\delta n_g = 2$.

Focusing on two equi-charge states near their degeneracy point at $n_g = 1$, the system can be described in terms of two states differing by one CP, $N_- = \pm 1$. Following Eq. 1.20 for a system with $2e$ periodic ground states, and under the assumption that $E_{1e} = 0$ gives an effective Hamiltonian in the states $|+1\rangle$ and $|-1\rangle$ of [48]:

$$H = H_t + H_C + H_{SC} = \begin{pmatrix} 2E_C n_g & \frac{1}{2}E_J \\ \frac{1}{2}E_J & -2E_C n_g \end{pmatrix} + E_C \quad (1.24)$$

with the eigenenergies:

$$E_{\pm, 2e} = E_C \pm \frac{1}{2}E_J \sqrt{E_C^2 + (4\frac{E_C}{E_J}(n_g - 1))^2}, \quad (1.25)$$

where $N_g = n_g - 1$.

The two hybridized energy bands are separated by an n_g -dependent gap. Therefore, the gate voltages V_{LPG} and V_{RPG} can tune the band gap of the system.

The energy splitting between the hybridized states as a function of n_g is:

$$\Delta E_{2e}(n_g) = E_+(n_g) - E_-(n_g) = \sqrt{(E_J)^2 + (4E_C(n_g - 1))^2} \quad (1.26)$$

Normalizing the energies with respect to Planck's constant h provides the fitting function to extract $E_J^* = \frac{E_J}{2}$ and $E_C^* = \frac{E_C}{2}$ using the applied excitation frequencies f_{2e} and corresponding resonance positions n_g [48]:

$$f_{2e}(n_g) = \sqrt{(E_J^*)^2 + (4E_C^*(n_g - 1))^2}. \quad (1.27)$$

The $\frac{E_C}{E_J}$ ratio determines the charge modulation [45]. Analogously to Eq. 1.16, Eq. 1.26 assumes $E_C \geq E_J$.

ΔE in Eq. 1.26 has a minimum at the charge state degeneracy ($n_g = 1$) where the mutual charging energy E_C is overcome and the energy splitting between the hybridized

eigenstates corresponds to E_J . Deviating from degeneracy leads to a n_g -dependent increases in ΔE . In the absence of coupling between the two islands ($E_J = 0$) Eq. 1.26 converges to a linear fit as the charge states no longer hybridize and anti-cross.

Measuring the RF reflectometry response as a function of the two island plunger gates reveals the honeycomb pattern characteristic for any generic double quantum dot (see Fig. 1.18 a). Each hexagon represents a discrete charge state associated with an even number of electrons on both islands. Based on cross-comparison with the Coulomb peak spacing observed for high magnetic fields (see Fig. 1.15) and high bias ($|eV_{SD}| > E_C$), the charge stability diagram at zero field was found to have $2e$ periodic Coulomb peak spacing on both superconducting islands.

Under microwave irradiation on the order of GHz applied to the RPG (see Sec. 1.3.3.2) the system demonstrates signatures of photon assisted inelastic Cooper pair tunneling across the Josephson junction (see Fig. 1.18 b). Microwave-induced resonances manifest themselves as additional lines parallel to the inter-island transition. This demonstrates that the mesoscopic superconducting islands are tunnel-coupled across the Josephson junction. PAT signatures are absent for both island-lead transitions indicative of the absence of CP tunneling between the islands and the normal leads. This is expected since a single state is not expected to anti-cross with the normal state continuum of the metallic leads. The observation of photon assisted tunneling demonstrates that the system can be coherently driven between charge states differing by one CP.

PAT allows to map the energy dispersion of the coupled system by applying a big range of frequencies. The inter-island charge state transition line is smeared out due to the hybridization of the two resonant charge states and could therefore not serve as a point of reference for the resonance peak position. Instead, the peak-to-peak spacings of PAT signals left and right of the inter-island transition were considered. They correspond to $2(n_g - 1)$ with respect to the even state degeneracy at $n_g = 1$ (see Fig. 1.18 c). The width of the PAT resonance peak – which also provides a measure of the inhomogeneous dephasing time [52] – was taken to be the error of uncertainty. A power-optimized frequency f range of 10-14 GHz in half-integer steps was considered for Fig. 1.18 d (see Appendix B).

Using Eq. 1.26 the energy splitting extracted for the charge state degeneracy position

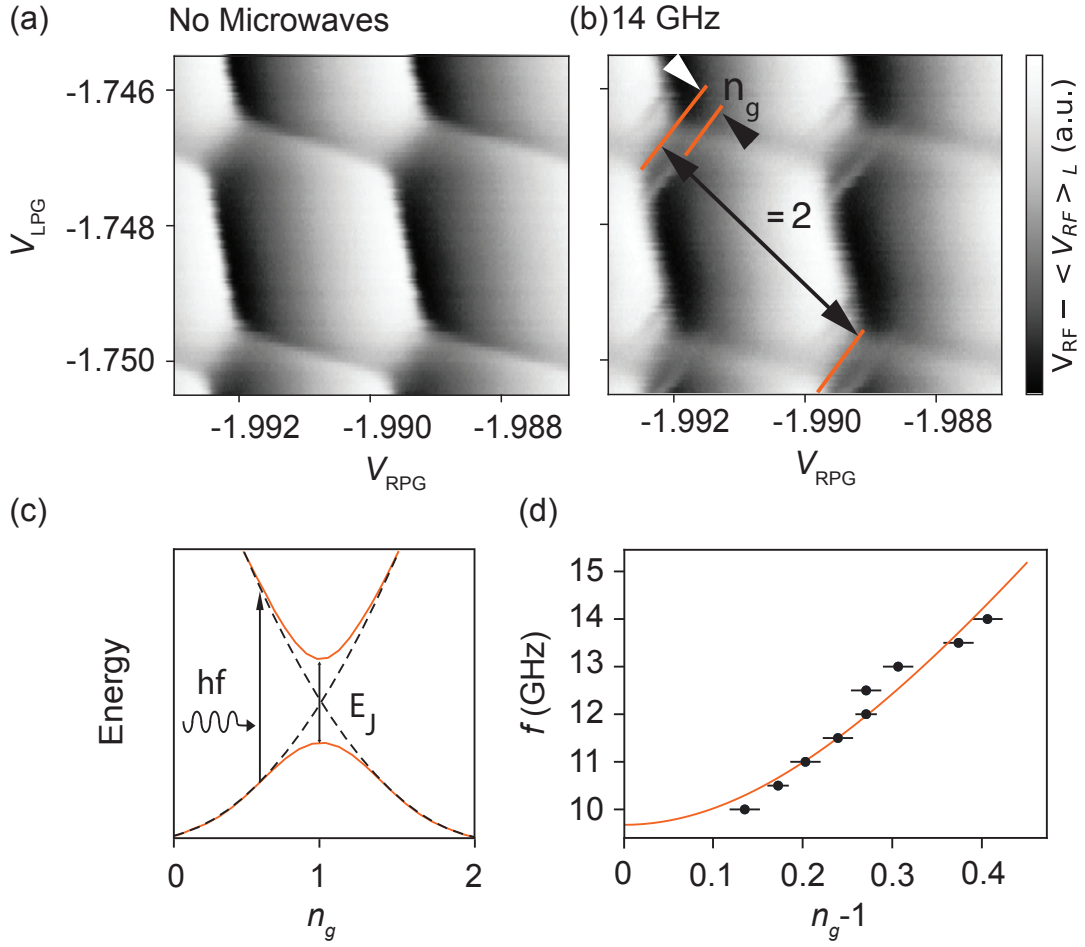


Figure 1.18: $2e$ periodic microwave-induced transitions in the absence of an external magnetic field. a) Charge stability diagram of mesoscopic superconducting double island with $2e$ periodic ground states. b) Under microwave irradiation photon assisted tunneling resonances appear parallel to the inter-island transition line shifted by n_g from the equi-charge state degeneracy. The degeneracy spacing is renormalized to 2. c) Schematic representation of coupled $2e$ periodic ground states with an avoided crossing which is equal to the Josephson coupling energy E_J at a degeneracy. d) Frequency dependence of the position of the PAT transition peak fitted with $f_{2e}(n_g) = \sqrt{(E_J^*)^2 + (4E_C^*(n_g - 1)^2)}$ to extract E_J^* and E_C^* .

at $n_g = 1$ was $\Delta E_{2e} = E_J = 40 \pm 1 \mu\text{eV}$. This corresponds to an excitation frequency of 9.7 ± 0.2 GHz. Further, a charging energy of $E_C = 27 \pm 1 \mu\text{eV}$ was extracted. E_J and E_C are of comparable scale which corresponds to a system with strong charge modulation [56].

After establishing photon assisted tunneling of CPs at $B=0$, microwaves were applied at 750 mT in an attempt to demonstrate $1e$ periodic transitions between zero energy

bound states in a hybrid system.

1.4.6 Photon Assisted Tunneling at Finite Magnetic field.

An axial magnetic field increased to 750 mT was shown to transition the system into a regime with a ZBP protected by a superconducting gap in S-I-S bias spectroscopy (see Fig. 1.13) in a $1e$ periodic regime (see Fig. 1.15).

As discussed, a topological phase transition and nucleation of MBSs left and right of the Josephson junction is one of the potential origins of a $1e$ periodic ground state at finite magnetic field (see Sec. 1.4.2). This work is focused on trying to probe the coupling E_M between γ_2 and γ_3 across the Josephson junction. The corresponding fermionic state can be occupied on the left or on the right island denoted by the odd eigenstates $|10\rangle$ and $|01\rangle$ as introduced in Sec. 1.2.2. Acknowledging the plurality of other physical phenomenas that can give rise to a ZBP in field, the two states are expressed in the charge state basis denoted by $|N_-\rangle = |0\rangle, |1\rangle$.

The effective Hamiltonian in the states $|0\rangle$ and $|1\rangle$ is [48]:

$$H = H_t + H_C + H_{SC} = \begin{pmatrix} E_C(n_g - \frac{1}{2}) & \frac{1}{2}E_{1e} \\ \frac{1}{2}E_{1e} & -E_C(n_g - \frac{1}{2}) \end{pmatrix} + \frac{1}{4}E_C. \quad (1.28)$$

Under the assumption of zero energy bound states on both islands the contribution of H_{SC} goes to zero since there no longer is an additional energy penalty attributed to single electron tunneling onto a superconducting island. The introduction of $1e$ periodic charge states shifts the degeneracies of the system to half integer values of n_g .

The corresponding eigenenergies are:

$$E_{\pm,1e}(n_g) = \frac{1}{4}E_C \pm \frac{1}{2}\sqrt{1 + (4\frac{E_{1e}}{E_C}(n_g - \frac{1}{2}))^2} \quad (1.29)$$

Still under the condition of $E_C \leq E_J$, an adapted energy splitting as a function of the gate induced charge n_g can be defined as:

$$\Delta E_{1e}(n_g) = E_{+,1e}(n_g) - E_{-,1e}(n_g) = \sqrt{(4E_C(n_g - \frac{1}{2}))^2 + (E_{1e})^2} \quad (1.30)$$

Again, renormalizing the energies with respect to h gives the fit function used to extract E_{1e}^* and E_C^* [48]:

$$f_{1e}(n_g) = \sqrt{(4E_C^*(n_g - \frac{1}{2}))^2 + (E_{1e}^*)^2} \quad (1.31)$$

Analogously to the $2e$ periodic charge states at $B=0$, the cross-coupling energy between two discrete $1e$ periodic charge states of a superconducting double island is also expected to open up an energy gap at the charge state degeneracy point if they arise from discrete bound states.

The Coulomb spacings observed in the charge stability diagram in Fig. 1.19 a are ≈ 1.7 mV and ≈ 1.4 mV for the left and the right island, respectively. This is roughly half the spacing observed at $B=0$, where Coulomb peak distances of ≈ 3.2 mV and ≈ 2.8 mV were observed (see Fig. 1.18 a). Both islands were therefore concluded to have $1e$ periodic ground states at 750 mT, which – as discussed in Sec. 1.4.3 – arises from discrete bound states.

Analogously to the E_J study at $B=0$ (see Sec. 1.4.5), the sample was irradiated with microwaves (10-14 GHz in half integer steps, see Appendix B) to extract the single electron mediated coupling strength E_{1e} . Signatures of PAT were observed parallel to the inter-island transition line (see Fig. 1.19 b). This solidifies the suspicion that the $1e$ periodicity arises from discrete zero energy bound states that tunnel-couple across the Josephson junction. The observation of PAT constitutes a demonstration of coherently driven superposed $1e$ periodic charge states in a hybrid system. As in the case of $2e$ PAT, microwave-induced resonances also exclusively appear on both sides of the inter-island transition and are absent for both island-lead transitions revealing that the probed coupling occurs across the Josephson junction.

Using Eq. 1.31 an energy splitting of $\Delta E = E_{1e} = 39 \pm 3 \mu\text{eV}$ was extracted for

the charge state degeneracy position at $n_g = \frac{1}{2}$ (see Fig. 1.19 d). This corresponds to an excitation frequency of 9.4 ± 0.6 GHz. The fit further provides an estimate of the charging energy of $E_C = 94 \pm 10 \mu\text{eV}$.

The extracted charging energy at 750 mT is significantly bigger than the one extracted at $B = 0$ ($E_{C,B=0} = 27 \pm 1 \mu\text{eV}$, see Sec 1.4.5). It is possible that the magnetic field modifies the charging energy by changing the capacitance. It could further be attributed to neglecting E_J in Eq. 1.31, which could have resulted in an overestimation of E_C .

The true nature of the investigated 1e periodic feature could not be determined. The 1e periodic charge states seem to have either emerged from ABSs or MBSs.

Coherently driving the 1e periodic system between two zero energy bound states at finited field constitutes an important step towards hybrid-based qubit experiments. An excitation signal with this frequency would drive the system exactly at the charge degeneracy point where it would have its longest coherence time. The energy splitting is therefore an important parameter for qubit operations. Attempts to realize a 1e periodic charge qubit in the presented device were unsuccessful. This could be attributed to the short coherence times of charge qubits associated with high charge noise fluctuations in the environment.

As mentioned, PAT has been observed in other solid state systems such as CP boxes [9] and gallium arsenide quantum dots [8], [7]. The observation of microwave-induced transitions – both 2e and 1e periodic – in a nanowire-based hybrid system has to the belief of the author not yet been reported.

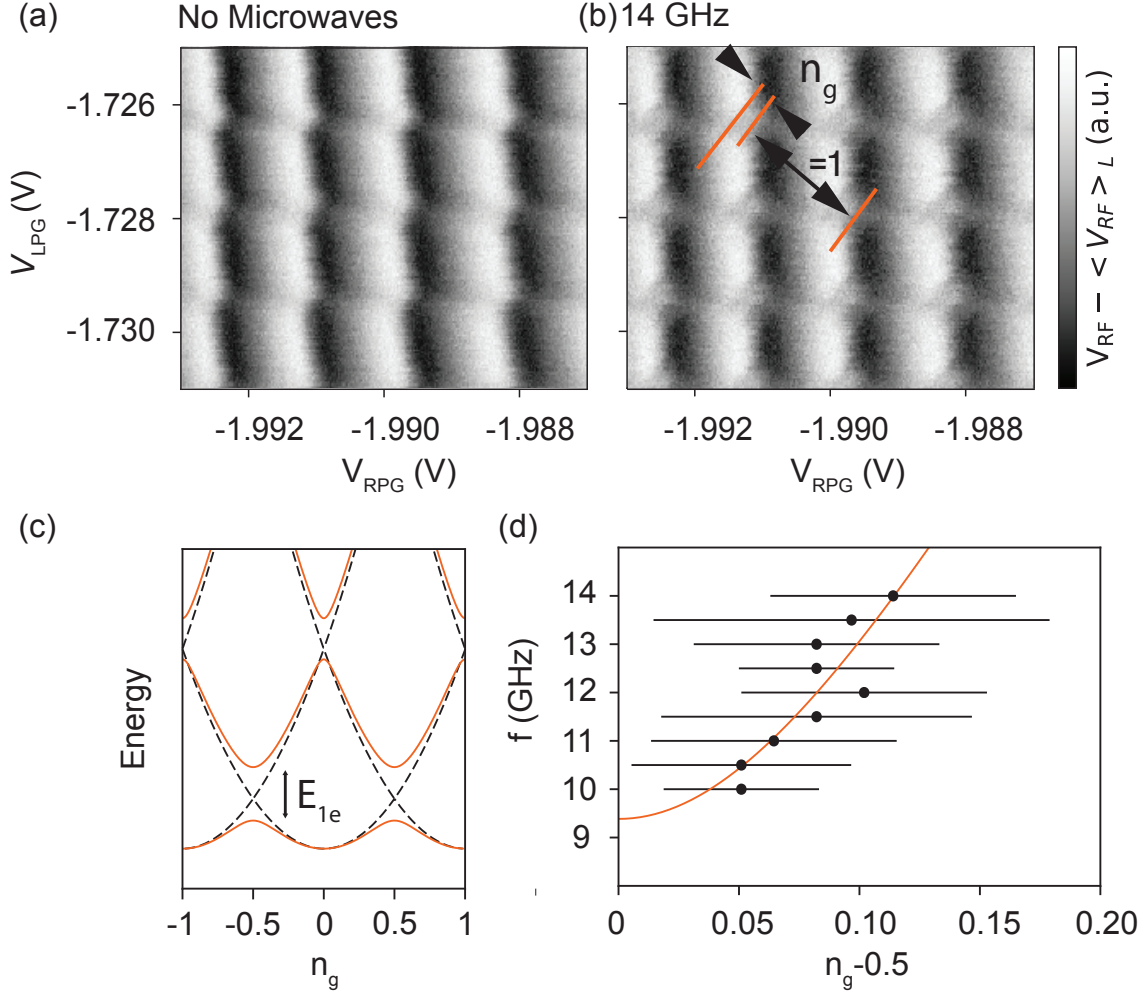


Figure 1.19: $1e$ periodic microwave-induced transitions at 750 mT: a) Charge stability diagram with $1e$ periodic Coulomb blockade. b) Under microwave irradiation charge transition peaks occur parallel to the inter-island transition line shifted by a distance n_g . The equi-charge state degeneracy spacing is renormalized to be 1. c) Schematic representation of coupled $1e$ periodic ground states with avoided crossing at degeneracy equal to the coupling energy E_{1e} . d) Frequency dependence of the position of the PAT transition peak is fitted with $f = \sqrt{(E_{1e}^*)^2 + (4E_C^*(n_g - 0.5)^2)}$ to extract the coupling strength E_{1e} .

1.5 Conclusion

This work summarizes experiments on a superconducting-semiconducting nanowire device in a mesoscopic double-island geometry. The measurements are focused on the coupling between states across a controllable tunnel barrier separating the two superconducting islands.

In the absence of an external magnetic field, a continuous microwave signal induced $2e$ periodic photon assisted tunneling (PAT) between the islands. The frequency dependence of the PAT transition peak allowed to extract a Josephson coupling energy of $E_J = 40 \pm 1 \mu\text{eV}$. Under an axial magnetic field, a splitting from a $2e$ to $1e$ periodic ground state was observed well before the closing of the superconducting gap. The transition from $2e$ to $1e$ periodic charge states *via* an even-odd Coulomb peak splitting is consistent with the emergence of bound states residing at zero energy. Both Majorana bound states and Andreev bound states would give rise to the presented results and therefore no distinction could be made. Tunneling bias spectroscopy in a superconducting-insulating-superconducting configuration in the $1e$ regime revealed a persistent zero bias peak in gate voltage separated from the quasiparticle continuum by a superconducting gap. The observation of photon assisted tunneling between $1e$ periodic states in that regime is interpreted as a demonstration of microwave-driven coherent transitions between two zero energy bound states. The extracted cross-junction coupling energy $E_{1e} = 39 \pm 3 \mu\text{eV}$ is an important step towards qubit experiments.

These measurements constitute the first reported observations of photon assisted Cooper pair and single electron tunneling in a semiconducting-superconducting hybrid system.

1.6 Outlook

Theoretical proposals [1], [2] and experimental results [3], [5], [6] make the hybrid system presented in this work a strong contender for hosting MBSs.

The extraction of the $1e$ exchange coupling strength provides important insight for operating a zero energy bound state charge qubit extending Nakamura *et. al.* work on a Cooper pair box charge qubit [27]. The qubit would be operated in Coulomb blockade ensuring that the charge occupation of the system is fixed. Two neighboring equi-charge states would act as the initialization and readout basis for the qubit. As discussed, the presence of an exchange coupling introduces an avoided crossing and coherently superposes the two states at charge state degeneracy. Pulsing the system non-adiabatically onto degeneracy of the two charge states *via* a plunger gate introduces a basis change to a superposed hybridized basis. For the duration of the pulse the system evolves. Pulsing back projects the system on one of the two charge states read out by the RF signal. In a coherent system, the charge state would oscillate as a function of the pulse duration [8], [27], [52]. As mentioned, attempts to demonstrate coherent control over the $1e$ system were unsuccessful. This could be partially contributed to fluctuations in the charge environment which could potentially be significantly improved by better filtering.

Apparent from the magnetic field evolution presented in Fig. 1.14, key limitation of the investigated double island geometry was the coupled tunability of E_J and E_{1e} . Both were controlled by the same experimental parameter, the middle cutter gate voltage V_{MCG} . This can be avoided in adapted triple island geometries where the Josephson coupling and bound state coupling are controlled *via* individual cutter gate voltages.

An additional limitation in the junction transmission control arises from accidental quantum dots in vicinity of the cutter gates presumably predominantly introduced in the wet etching. By extension, this also limits the control over the cross-junction coupling. A potential solution is a sophisticated growth technique referred to as shadow junctions, where Al is selectively deposited using neighboring nanowires as shadow masks [57]. The three-dimensional mask is created *via* trenches where the nanowires grow perpendicular to the two sloped trench walls in a precursor-defined staggered arrays. Neighboring nanowires thereby act as the shadow template negating the etching step.

Hybrid nanowire based qubit experiments constitute an important milestone prove of principle of Majorana-based qubits. However, to ultimately implement a scalable approach to topological quantum computing nanowires do not provide a suitable basis.

Theoretical proposals for complex two-dimensional quantum networks for scalable designs [58],[59] appear more feasible in other materials such as selective area growth and two-dimensional electron gases. Arbitrarily complex quantum networks can be defined. Selective area growth was only recently experimentally realized [60] and still requires more characterization. Recent advances in material science have lead to the observation of signatures consistent with Majorana zero modes in proximitized two-dimensional electron gases [61].

Appendices

A Fabrication of Double Island Device

A.0 Blank Substrate

The devices were fabricated on semi-conducting wafers consisting of highly purified Si (525 μm) capped by a thermal silicon oxide layer (80 nm) provided by *TOPSIL*. A local back-gate (Ti 5 nm, Au 35 nm) was then deposited to tune the global density of the device. Local back-gates were chosen over global ones to avoid attenuation of the input electromagnetic waves. The metal was passivated globally by an electrically insulating bi-layer consisting of silicon nitride (Si_3N_4) (200 nm) grown by plasma enhanced chemical vapor deposition and capped locally with hafniumdioxide (HfO_2) (15 nm). On top of the passivated surface golden meander-structures (100 nm) terminated as circular so called bonding pads were patterned using UV-lithography masks. They constituted the interface between the patterned device and the daughterboard. Rotary gold evaporation with a sample tilt of 12°degrees with respect to the incoming metal vapor introduced a slope in the meander profile. This supported a continuous overlap with metallic electrodes, which were evaporated in subsequent fabrication steps. Alignment marks functioning as reference points for further process steps were defined via an *Elionix* electron beam lithograph (EBL) setup to achieve optimal accuracy. The fabrication steps for these blank substrates were performed by Shivendra Upadhyay.

A.1 Device Fabrication

Cleaning substrate surface

- Submerging into NMP (80°C, 20 min).
- Sonicating in NMP (80 kHz, 1 min).

Comment: This is the only step where sonication of the wafer to remove residues from the surface is recommended. After the nanowire deposition there is a risk of damaging the device.

- Rinsing in acetone, IPA and Milli-Q before drying with N_2 .
- O_2 plasma etching (4 min) to reduce organic residues from the surface.

Nanowire deposition

InAs nanowires (growth batch *qdev578*) with two neighboring facets of epitaxially grown Al were broken off the substrate by stroking over the nanowire growth substrate with a small triangular piece of a cleanroom wipe. The wires lying on the substrate were then transferred onto a pre-processed silicon blank substrate by means of a grounded semi-automatic micro manipulator. A controllable needle with a diameter of $0.1\ \mu\text{m}$ was brought into close proximity to one end of the nanowire until one end stuck to the needle allowing for transfer of the one-dimensional crystal. To deposit the nanowire attached to the needle the nanowire was brought into contact with the device substrate to which it stuck when the needle was carefully removed.

Comment: A angle of approximately 15° degrees with respect to the substrate plane is recommended for more targeted pick-up of the wire avoiding accidental accumulation of additional wires at the needle. Grounding of the stage hosting the growth and device substrates and needle are important to avoid destructive discharging events.

Aluminum Etching

Aluminum was selectively removed by wet-etching with Transene-D in windows defined by electron-beam lithography.

- Resist: EL9 (spincoating: $10\ \mu\text{L}$, 45 sec, 4500 rpm), bake on hotplate (185°C , 2 min).

Comment: Double A6 might be better, more viscous and therefore wrapping the wire better. Hence etching over-run would be minimized.

- Electron beam lithography: (240000 pt, $600\ \mu\text{m}$, 500 pA) 0.12 dose chef. $\rightarrow 1120\ \mu\text{C}/\text{cm}^2$ dose
- Develop: MIBK:IPA 1:3 (1 min), rinsing in IPA, N_2
- Postbake on hotplate (30 sec, 12°C)
- The etchant Transene-D was heated in a heat bath (50°C). The temperature was monitored in a reference Milli-Q beaker sitting in the same heatbath. The sample was submerged into the Transene-D (9 sec including transfer to a MQ

beaker also kept at 50° C). The sample was then transferred to three more Milli-Q beakers at room temperatures to perform a dilution series (30 sec, 30 sec, 3 min). *Comment: As soon as vacuum is broken after the wire growth, the indium arsenide and aluminum react with atmospheric oxygen and forms a native oxide layer. The etching of aluminum is hard to control, since the etching rate for the native aluminum oxide is smaller than for pure aluminum. Based on experimental investigation conducted prior to this work an etching time of 9 seconds was chosen.*

- Strip resist before scanning electron micrograph imaging: acetone (10 min), IPA 1 min, N₂, O₂ Plasma ash (4 min).

Ohmic contacts

- Resists: Spin-coating with A4 (10 μ L, 45 sec, 4500 rpm), baking (115° C, 2 min). Spin-coating with A6 (10 μ L, 45 sec, 4500 rpm, 2 min, 115° C).
- Electron beam lithography: Splitting design into fine/coarse contacts for subsequent exposure (240000 pt/ 600 μ m, 500 pA) 0.14 dose chef. -> 1120 μ C/cm² dose.

Comment: Breaking up the design into fine and coarse features is done to optimize the alignment of fine features at the device. All fine features can thereby be written immediately after field-corrections. The more coarse features take longer to write and are therefore subjected to bigger stage drifts.

- Develop: MIBK:IPA 1:3 (80 sec), rinsing in IPA, N₂, O₂ ashing (1min).
- Metal evaporation: Metalization (5 nm Ti, 150 nm Au) done in AJA system with preliminary RF milling (15 W, 5 min, 18 mTorr, 30 sccm).
- Liftoff in NMP (45 min, 80° C), pipetting, Acetone, IPA, N₂, O₂ ashing (2 min).

ALD window

- Resist: Spin EL6 (10 μ L, 45 sec, 4500 rpm), bake (115° C, 2 min) to create an undercut to reduce the ALD walls Spin A2 (10 μ L, 45 sec, 4500 rpm, 2 min, 115° C).
- Design: Wecas: Expose: (20000 pt/ 300 μ m, 3.7 nA) 0.72 dose coefficient -> 1180 μ C/cm² dose for main window + 0.28 dose coefficient -> 460 μ C/cm² dose for 300 nm undercut around the perimeter.

- Develop: MIBK:IPA 1:3 (1 min), rinsing in IPA, N₂, O₂ ashing (1 min).
- Atomic layer deposition growth of 7 nm of hafniumdioxide (HfO₂). This step seals off the device from the atmosphere. Therefore, it is important to remove any residues from it before the deposition process starts. This was done by plasma ashing the sample for 60 s before loading it in the ALD growth chamber. The sample was left inside outgassing for (90° deg, 10 hours) (HfO₂: pulse time 0.6 sec, H₂O: 0.02 sec)

Comment: Scratching the edges of device substrates with a metallic syringe provides more interface to facilitate easier ALD liftoff. Caution has to be taken not to damage the alignment marks used for future lithographic exposures.

- Liftoff: NMP (80° C for 1,5 h) using N₂ gun and pipette to accelerate liftoff.

Gates

- Spin-coat resist: Double layer of A4 baking with 2 min at 115° C after each layer.
- Preparing lithography mask.
- Electron beam lithography: fine/coarse contacts (240000 pt/ 600 μm, 500 pA) 0.14 dose chef. -> 1120 μC/cm² dose.
- Elionix: Letting the sample thermally stabilize in the Elionix chamber for 30 min before starting the exposure.
- Lithography mask development: Submerging in MIBK:IPA (1:3) (1 min) rinsing in IPA, drying with N₂ gun, O₂ ash (1 min).
- Metal evaporation: Ti (5 nm) while rotating the sample stage, Au (160 nm in total) all while rotating sample stage. To ensure continuous crawl-on of the wrapper-gate electrodes, part of the evaporation was conducted with a tilt of the sample stage. The sequence went: 60 nm 0° tilt, 15 nm with 5° degrees tilt and subsequently 85 nm without tilt.)
- Liftoff: NMP (76° C, 1 h).

Comment: Using pipettes of different sizes can be used to create friction on the sample surface to facilitate better liftoff.

B Photon assisted tunneling

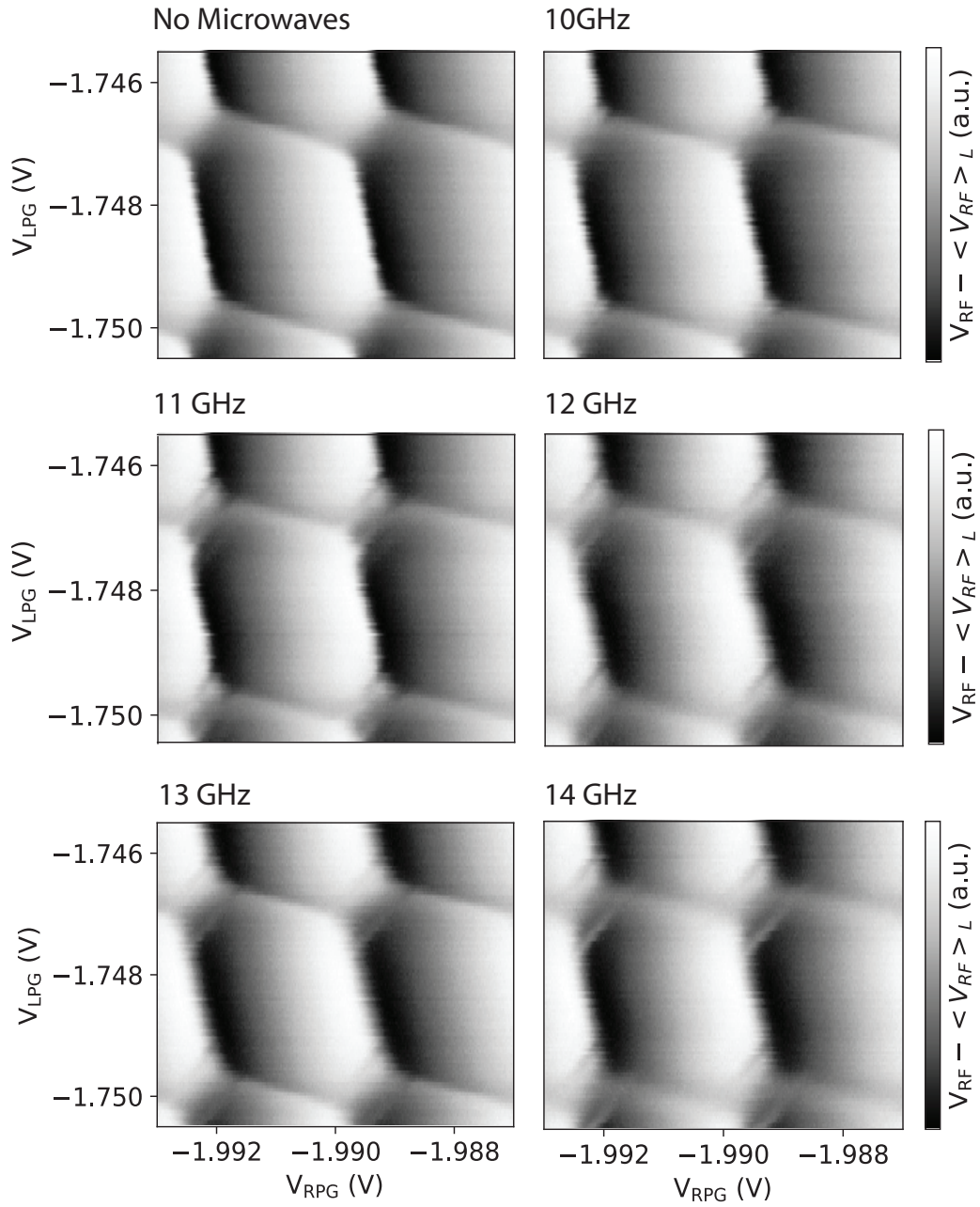


Figure 20: 2e PAT for different frequencies.

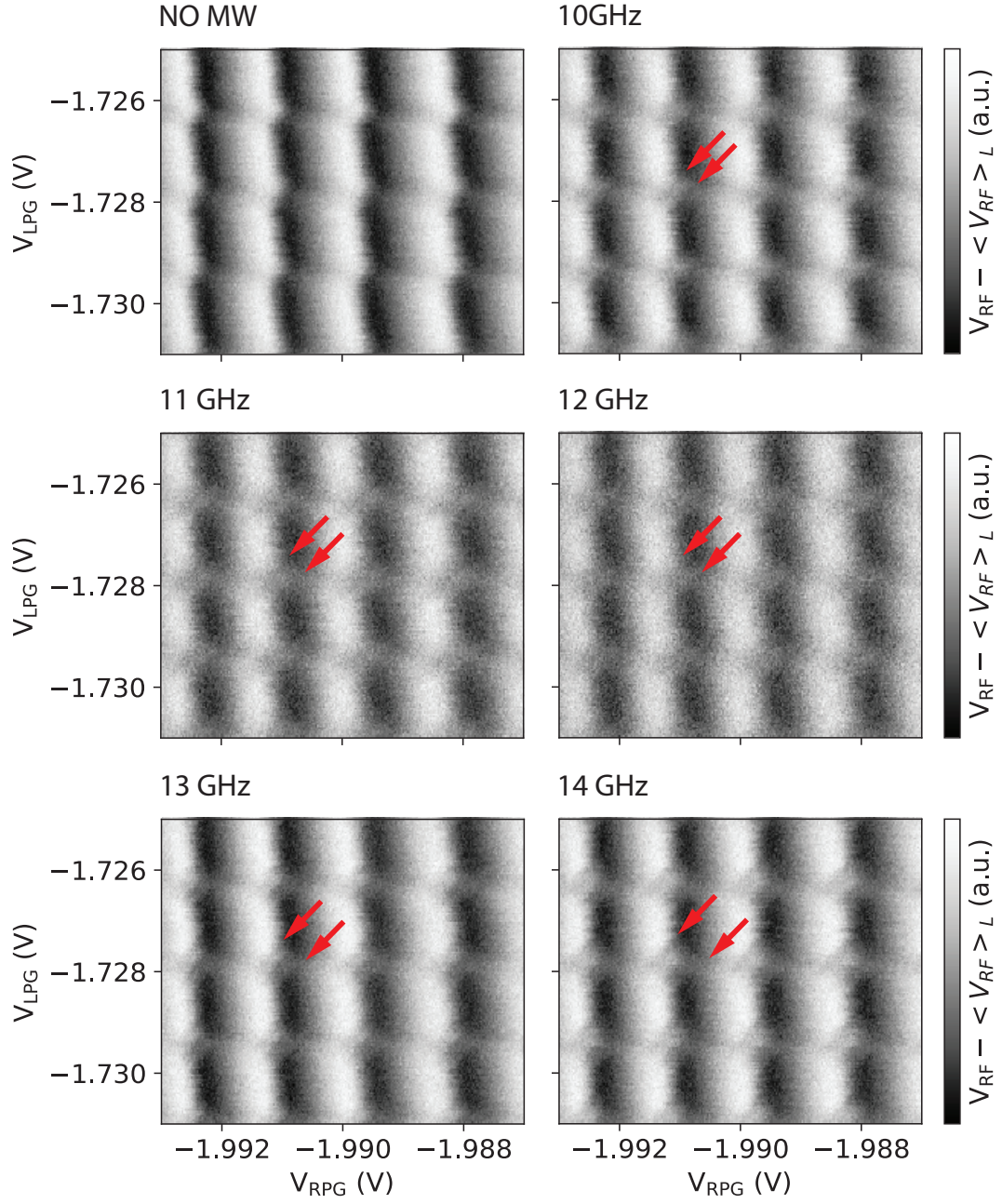


Figure 21: 1e PAT for different frequencies.

Bibliography

- [1] R. M. Lutchyn, J. D. Sau, and S. Das Sarma, “Majorana Fermions and a Topological Phase Transition in Semiconductor-Superconductor Heterostructures,” *Physical Review Letters*, vol. 105, p. 077001, 8 2010.
- [2] Y. Oreg, G. Refael, and F. von Oppen, “Helical Liquids and Majorana Bound States in Quantum Wires,” *Physical Review Letters*, vol. 105, p. 177002, 10 2010.
- [3] V. Mourik, K. Zuo, S. M. Frolov, S. R. Plissard, E. P. A. M. Bakkers, and L. P. Kouwenhoven, “Signatures of Majorana fermions in hybrid superconductor-semiconductor nanowire devices,” *Science (New York, N.Y.)*, vol. 336, pp. 1003–7, 5 2012.
- [4] M. T. Deng, C. L. Yu, G. Y. Huang, M. Larsson, P. Caroff, and H. Q. Xu, “Anomalous Zero-Bias Conductance Peak in a Nb–InSb Nanowire–Nb Hybrid Device,” *Nano Letters*, vol. 12, pp. 6414–6419, 12 2012.
- [5] M. T. Deng, S. Vaitiekėnas, E. B. Hansen, J. Danon, M. Leijnse, K. Flensberg, J. Nygård, P. Krogstrup, and C. M. Marcus, “Majorana bound state in a coupled quantum-dot hybrid-nanowire system,” *Science (New York, N.Y.)*, vol. 354, pp. 1557–1562, 12 2016.
- [6] H. Zhang, C.-X. Liu, S. Gazibegovic, D. Xu, J. A. Logan, G. Wang, N. van Loo, J. D. S. Bommer, M. W. A. de Moor, D. Car, R. L. M. Op het Veld, P. J. van Veldhoven, S. Koelling, M. A. Verheijen, M. Pendharkar, D. J. Pennachio, B. Shojaei, J. S. Lee, C. J. Palmstrøm, E. P. A. M. Bakkers, S. D. Sarma, and L. P. Kouwenhoven, “Quantized Majorana conductance,” *Nature*, vol. 556, pp. 74–79, 3 2018.

-
- [7] L. P. Kouwenhoven, S. Jauhar, J. Orenstein, P. L. McEuen, Y. Nagamune, J. Motohisa, and H. Sakaki, "Observation of Photon-Assisted Tunneling through a Quantum Dot," *Physical Review Letters*, vol. 73, pp. 3443–3446, 12 1994.
- [8] J. R. Petta, A. C. Johnson, C. M. Marcus, M. P. Hanson, and A. C. Gossard, "Manipulation of a Single Charge in a Double Quantum Dot," *Physical Review Letters*, vol. 93, p. 186802, 10 2004.
- [9] Y. Nakamura, C. D. Chen, and J. S. Tsai, "Spectroscopy of Energy-Level Splitting between Two Macroscopic Quantum States of Charge Coherently Superposed by Josephson Coupling," *Physical Review Letters*, vol. 79, pp. 2328–2331, 9 1997.
- [10] G. E. Moore, "Cramming More Components onto Integrated Circuits," tech. rep.
- [11] R. P. Feynman, "Quantum mechanical computers," *Foundations of Physics*, vol. 16, pp. 507–531, 6 1986.
- [12] D. Loss and D. DiVincenzo, "Quantum information is physical," *Superlattices and Microstructures*, vol. 23, pp. 419–432, 3 1998.
- [13] M. Leijnse and K. Flensberg, "Introduction to topological superconductivity and Majorana fermions," *Semiconductor Science and Technology*, vol. 27, p. 124003, 12 2012.
- [14] J. Alicea, "Majorana fermions in a tunable semiconductor device," *Physical Review B*, vol. 81, p. 125318, 3 2010.
- [15] A. Y. Kitaev, "Unpaired Majorana fermions in quantum wires," *Physics-Uspekhi*, vol. 44, pp. 131–136, 10 2001.
- [16] J. Bardeen, L. N. Cooper, and J. R. Schrieffer, "Theory of Superconductivity," *Physical Review*, vol. 108, pp. 1175–1204, 12 1957.
- [17] M. Tinkham, *Introduction to superconductivity*. Dover Publications, 2004.
- [18] A. Manchon, H. C. Koo, J. Nitta, S. M. Frolov, and R. A. Duine, "New perspectives for Rashba spin–orbit coupling," *Nature Materials* 2015 14:9, vol. 14, p. 871, 8 2015.
- [19] T. Ihn, *Semiconductor Nanostructures*. Oxford University Press, 11 2009.
- [20] B. Pannetier and H. Courtois, "Andreev Reflection and Proximity effect," 12 1999.

-
- [21] S. Vaitiekėnas, M. T. Deng, J. Nygård, P. Krogstrup, and C. M. Marcus, "Effective g-factor in Majorana Wires," 10 2017.
 - [22] G. E. Blonder, M. Tinkham, and T. M. Klapwijk, "Transition from metallic to tunneling regimes in superconducting microconstrictions: Excess current, charge imbalance, and supercurrent conversion," *Physical Review B*, vol. 25, pp. 4515–4532, 4 1982.
 - [23] S. D. Sarma, M. Freedman, and C. Nayak, "Majorana Zero Modes and Topological Quantum Computation," 1 2015.
 - [24] M. T. Deng, S. Vaitiekėnas, E. Prada, P. San-Jose, J. Nygård, P. Krogstrup, R. Aguado, and C. M. Marcus, "Majorana non-locality in hybrid nanowires," 12 2017.
 - [25] C.-X. Liu, J. D. Sau, T. D. Stanescu, and S. Das Sarma, "Andreev bound states versus Majorana bound states in quantum dot-nanowire-superconductor hybrid structures: Trivial versus topological zero-bias conductance peaks," *Physical Review B*, vol. 96, p. 075161, 8 2017.
 - [26] A. F. Andreev, "Thermal conductivity of the intermediate state of superconductors. II," Tech. Rep. 6, 1965.
 - [27] Y. Nakamura, Y. A. Pashkin, and J. S. Tsai, "Coherent control of macroscopic quantum states in a single-Cooper-pair box," *Nature*, vol. 398, pp. 786–788, 4 1999.
 - [28] A. A. Houck, J. A. Schreier, B. R. Johnson, J. M. Chow, J. Koch, J. M. Gambetta, D. I. Schuster, L. Frunzio, M. H. Devoret, S. M. Girvin, and R. J. Schoelkopf, "Controlling the Spontaneous Emission of a Superconducting Transmon Qubit," *Physical Review Letters*, vol. 101, p. 080502, 8 2008.
 - [29] L. Bretheau, "Localized excitations in superconducting atomic contacts: probing the Andreev doublet," 2013.
 - [30] J. Pillet, "Tunneling spectroscopy of the Andreev Bound States in a Carbon Nanotube," 2011.

-
- [31] J.-D. Pillet, C. H. L. Quay, P. Morfin, C. Bena, A. L. Yeyati, and P. Joyez, “Andreev bound states in supercurrent-carrying carbon nanotubes revealed,” *Nature Physics* 2010 6:12, vol. 6, p. 965, 11 2010.
 - [32] T. Dirks, T. L. Hughes, S. Lal, B. Uchoa, Y.-F. Chen, C. Chialvo, P. M. Goldbart, and N. Mason, “Transport through Andreev bound states in a graphene quantum dot,” *Nature Physics*, vol. 7, pp. 386–390, 5 2011.
 - [33] M. Leijnse and K. Flensberg, “Scheme to measure Majorana fermion lifetimes using a quantum dot,” *RAPID COMMUNICATIONS PHYSICAL REVIEW B*, vol. 84, no. 4, pp. 140501–140502, 2011.
 - [34] J. R. Petta, A. C. Johnson, C. M. Marcus, M. P. Hanson, and A. C. Gossard, “Manipulation of a Single Charge in a Double Quantum Dot,” vol. 2123, no. 73.
 - [35] W. G. Van Der Wiel, S. De Franceschi, J. M. Elzerman, T. Fujisawa, S. Tarucha, and L. P. Kouwenhoven, “Electron transport through double quantum dots,” 2002.
 - [36] T. H. Oosterkamp, T. Fujisawa, W. G. van der Wiel, K. Ishibashi, R. V. Hijman, S. Tarucha, and L. P. Kouwenhoven, “Microwave spectroscopy of a quantum-dot molecule,” *Nature*, 1998.
 - [37] T. H. Stoof and Y. V. Nazarov, “Time-dependent resonant tunneling via two discrete states,” *Physical Review B*, vol. 53, pp. 1050–1053, 1 1996.
 - [38] A. E. Antipov, A. Bargerbos, G. W. Winkler, B. Bauer, E. Rossi, and R. M. Lutchyn, “Effects of gate-induced electric fields on semiconductor Majorana nanowires,” 1 2018.
 - [39] R. S. Wagner and W. C. Ellis, “Vapor-liquid-solid mechanism of single crystal growth,” *Citation: Appl. Phys. Lett*, vol. 4, no. 89, 1964.
 - [40] W. Chang, S. M. Albrecht, T. S. Jespersen, F. Kuemmeth, P. Krogstrup, J. Nygård, and C. M. Marcus, “Hard gap in epitaxial semiconductor–superconductor nanowires,” *Nature Nanotechnology*, vol. 10, pp. 232–236, 3 2015.
 - [41] F. Pobell, *Matter and methods at low temperatures*. Springer, 2007.
 - [42] C. Barthel, M. Kjørgaard, J. Medford, M. Stopa, C. M. Marcus, M. P. Hanson, and A. C. Gossard, “Fast sensing of double-dot charge arrangement and spin state

-
- with a radio-frequency sensor quantum dot," *Physical Review B*, vol. 81, p. 161308, 4 2010.
- [43] C. Barthel, "Control and fast measurement of spin qubits," 2010.
- [44] D. J. Reilly, C. M. Marcus, M. P. Hanson, and A. C. Gossard, "Fast single-charge sensing with a rf quantum point contact," *Applied Physics Letters*, vol. 91, p. 162101, 10 2007.
- [45] A. A. Houck, J. Koch, M. H. Devoret, S. M. Girvin, and R. J. Schoelkopf, "Life after charge noise: recent results with transmon qubits," *Quantum Information Processing*, vol. 8, pp. 105–115, 6 2009.
- [46] S. Albrecht, E. Hansen, A. Higginbotham, F. Kuemmeth, T. Jespersen, J. Nygård, P. Krogstrup, J. Danon, K. Flensberg, and C. Marcus, "Transport Signatures of Quasiparticle Poisoning in a Majorana Island," *Physical Review Letters*, vol. 118, p. 137701, 3 2017.
- [47] S. M. Albrecht, A. P. Higginbotham, M. Madsen, F. Kuemmeth, T. S. Jespersen, J. Nygård, P. Krogstrup, and C. M. Marcus, "Exponential protection of zero modes in Majorana islands," *Nature*, vol. 531, pp. 206–209, 3 2016.
- [48] D. van Zanten, D. Sabonis, J. Suter, D. I. Pikulin, J. Vayrynen, E. O'Farrell, D. Razmadze, K. D. Petersson, P. Krogstrup, and C. M. Marcus, "Unpublished," 2018.
- [49] C. A. Stafford and N. S. Wingreen, "Resonant Photon-Assisted Tunneling through a Double Quantum Dot: An Electron Pump from Spatial Rabi Oscillations," tech. rep., 1996.
- [50] T. Hayashi, T. Fujisawa, H. D. Cheong, Y. H. Jeong, and Y. Hirayama, "Coherent Manipulation of Electronic States in a Double Quantum Dot," *Physical Review Letters*, vol. 91, p. 226804, 11 2003.
- [51] J. Gorman, D. G. Hasko, and D. A. Williams, "Charge-Qubit Operation of an Isolated Double Quantum Dot," *Physical Review Letters*, vol. 95, p. 090502, 8 2005.

-
- [52] K. D. Petersson, J. R. Petta, H. Lu, and A. C. Gossard, "Quantum Coherence in a One-Electron Semiconductor Charge Qubit," *Physical Review Letters*, vol. 105, p. 246804, 12 2010.
 - [53] Y. Nakamura, C. D. Chen, and J. S. Tsai, "Spectroscopy of Energy-Level Splitting between Two Macroscopic Quantum States of Charge Coherently Superposed by Josephson Coupling," *Physical Review Letters*, vol. 79, pp. 2328–2331, 9 1997.
 - [54] Y. A. Pashkin, T. Yamamoto, O. Astafiev, Y. Nakamura, D. V. Averin, and J. S. Tsai, "Quantum oscillations in two coupled charge qubits," *Nature*, vol. 421, pp. 823–826, 2 2003.
 - [55] Y. A. Pashkin, O. Astafiev, T. Yamamoto, Y. Nakamura, and J. S. Tsai, "Josephson charge qubits: a brief review," *Quantum Information Processing*, vol. 8, pp. 55–80, 6 2009.
 - [56] J. Koch, T. M. Yu, J. Gambetta, A. A. Houck, D. I. Schuster, J. Majer, A. Blais, M. H. Devoret, S. M. Girvin, and R. J. Schoelkopf, "Charge-insensitive qubit design derived from the Cooper pair box," *Physical Review A*, vol. 76, p. 042319, 10 2007.
 - [57] S. Gazibegovic, D. Car, H. Zhang, S. C. Balk, J. A. Logan, M. W. A. de Moor, M. C. Cassidy, R. Schmits, D. Xu, G. Wang, P. Krogstrup, R. L. M. Op het Veld, K. Zuo, Y. Vos, J. Shen, D. Bouman, B. Shojaei, D. Pennachio, J. S. Lee, P. J. van Veldhoven, S. Koelling, M. A. Verheijen, L. P. Kouwenhoven, C. J. Palmstrøm, and E. P. A. M. Bakkers, "Epitaxy of advanced nanowire quantum devices," *Nature*, vol. 548, pp. 434–438, 8 2017.
 - [58] J. Alicea, Y. Oreg, G. Refael, F. von Oppen, and M. P. A. Fisher, "Non-Abelian statistics and topological quantum information processing in 1D wire networks," *Nature Physics*, vol. 7, pp. 412–417, 5 2011.
 - [59] T. Karzig, C. Knapp, R. M. Lutchyn, P. Bonderson, M. B. Hastings, C. Nayak, J. Alicea, K. Flensberg, S. Plugge, Y. Oreg, C. M. Marcus, and M. H. Freedman, "Scalable designs for quasiparticle-poisoning-protected topological quantum computation with Majorana zero modes," *Physical Review B*, vol. 95, p. 235305, 6 2017.
 - [60] F. Krizek, J. E. Sestoft, P. Aseev, S. Marti-Sanchez, S. Vaitiekėnas, L. Casparis, S. A. Khan, Y. Liu, T. Stankevič, A. M. Whiticar, A. Fursina, F. Boekhout,

- R. Koops, E. Uccelli, L. P. Kouwenhoven, C. M. Marcus, J. Arbiol, and P. Krogstrup, "Field effect enhancement in buffered quantum nanowire networks," 2 2018.
- [61] F. Nichele, A. C. Drachmann, A. M. Whiticar, E. C. O'Farrell, H. J. Suominen, A. Fornieri, T. Wang, G. C. Gardner, C. Thomas, A. T. Hatke, P. Krogstrup, M. J. Manfra, K. Flensberg, and C. M. Marcus, "Scaling of Majorana Zero-Bias Conductance Peaks," *Physical Review Letters*, vol. 119, p. 136803, 9 2017.